Climate simulations of the Permian-Triassic boundary: Ocean acidification and the extinction event

A. Montenegro,[1,2] P. Spence,[3] K. J. Meissner,[3] M. Eby,[4] M. J. Melchin,[1] and S. T. Johnston[4]

Received 23 September 2010; revised 25 April 2011; accepted 5 May 2011; published 2 August 2011.

[1] The causes for the Permian-Triassic Boundary (PTB) extinction, the largest mass extinction on record, remain enigmatic. The period is marked by large-scale volcanic eruptions and evidence for widespread ocean anoxia, which have led to suggestions that these events generated, or played a part in, the extinction. Furthermore, hypercapnia and ocean acidification caused by volcanic emissions of CO_2 and CH_4 have been put forward as potential kill mechanisms. We present the first PTB climate simulations in which ocean acidity is evaluated directly with a coupled climate-carbon cycle model. The experiments also address the sensitivity of ocean circulation and oxygen levels to uncertainties in paleogeography and to different bottom topographies. Modeled temperature and precipitation-evaporation are in good agreement with reconstructions and climate-sensitive sediments. There is also good agreement between modeled vegetation and reconstructed biomes. The reduction in ocean pH brought about by the increase in atmospheric CO_2 is biologically significant. Aragonite saturation levels are low enough to make the whole ocean unsuitable to aragonitic species, and large areas of the ocean become unsaturated in relationship to calcite. No general bottom anoxia is reproduced. Modeled deep ocean O_2 concentrations are not significantly impacted by changes in paleogeography and bathymetry, an indication that in our model a change in ocean dynamics resulting from climate warming is not sufficient by itself to generate widespread anoxic conditions during the period.

Citation: Montenegro, A., P. Spence, K. J. Meissner, M. Eby, M. J. Melchin, and S. T. Johnston (2011), Climate simulations of the Permian-Triassic boundary: Ocean acidification and the extinction event, *Paleoceanography*, *26*, PA3207, doi:10.1029/2010PA002058.

1. Introduction

[2] The boundary between the Permian and Triassic periods marks the occurrence of the largest extinction event preserved in the geological record. At 251.4 million years before present (Ma) [*Bowring et al.*, 1998], about 90% of marine species and 70% of land vertebrate families disappear [*Erwin*, 1994] and there were large changes in land plant species abundance and community structure [*McElwain*, 2007]. The Permian-Triassic Boundary (PTB) event is also the only mass extinction known to significantly impact insects [*Erwin*, 1994].

[3] The breadth and magnitude of the extinction are not widely debated. It is also agreed that the PT boundary is marked by a large and rapid negative excursion of the oceanic $\delta^{13}C$ record and that the extinction occurred at the same time as large scale volcanic eruptions of the Siberian Traps. There is much less consensus on the other aspects of the event. The change in $\delta^{13}C$ is interpreted by some as associated with the causes [*Berner*, 2002] and by others with the consequences [*Twitchett et al.*, 2001] of the biotic crisis. Estimates of the duration of the extinction and environmental perturbation range from more than five million years [*Yin et al.*, 2007] to less than 60 thousand years [*Rampino et al.*, 2000].

[4] There is also little agreement on what caused the extinction itself (for a more comprehensive review of the causes of the PTB extinction see *Wignall* [2007] and *Erwin* [1994]). Given the synchronicity with the Siberian Traps, a number of proposed extinction causes are related to extensive volcanism. These include mantle mega-plumes inducing the release of methane along continental margins [*Heydari et al.*, 2008], ocean acidification caused by high atmospheric CO_2 concentrations [*Heydari et al.*, 2003; *Payne et al.*, 2007], acid rain and global cooling [*Campbell et al.*, 1992].

[1]Department of Earth Sciences, St. Francis Xavier University, Antigonish, Nova Scotia, Canada.
[2]Environmental Sciences Research Centre, St. Francis Xavier University, Antigonish, Nova Scotia, Canada.
[3]Climate Change Research Centre, University of New South Wales, Sydney, New South Wales, Australia.
[4]School of Earth and Ocean Sciences, University of Victoria, Victoria, British Columbia, Canada.

Copyright 2011 by the American Geophysical Union.
0883-8305/11/2010PA002058

[5] There are several geological indications of widespread deep ocean anoxia during and prior to the extinction event [*Wignall*, 2007; *Wignall et al.*, 2010; *Kato et al.*, 2002], and a series of proposed extinction mechanisms take this into consideration. Among these are hypercapnia due to overturning of previously stagnant oceans [*Knoll et al.*, 1996], escape of hydrogen sulfide from an euxinic ocean, which would cause both direct poisoning and damage to the ozone layer [*Kump et al.*, 2005] and anoxic conditions extending to shallow waters [*Wignall and Twitchett*, 1996]. Some studies point to a possible link between ocean anoxia and extensive volcanism, with the ocean becoming stagnant and anoxic due to global warming induced by the release of CO_2 and CH_4 by volcanic activity [*Wignall*, 2007].

[6] Here we use a climate model to evaluate parameters which have been directly or indirectly linked to the PTB extinction. While our experiments are not designed as proxies of the extinction event itself, our equilibrium results of the PTB can be used to assess two mechanisms associated with the extinction: ocean anoxia and ocean acidification due to high CO_2 atmospheric concentrations.

[7] Numerical simulations of the PTB have been conducted by models that can be broadly arranged in three groups: (1) uncoupled models, (2) Earth system models of intermediate complexity (EMIC), and (3) atmosphere-ocean general circulation models (AOGCM).

[8] 1. Uncoupled models include models with a 3D atmosphere but a simple 2D "surface slab" ocean component. In some cases ocean temperature is prescribed and in others it is allowed to vary via exchanges with the atmosphere. These models do not calculate ocean circulation or any subsurface field, which limit their relevance to our study [*Kutzbatch and Ziegler*, 1993; *Fluteau et al.*, 2001; *Gibbs et al.*, 2002].

[9] Another category of uncoupled models are models that have a 3D ocean component but no atmosphere. In these cases the ocean model is forced with prescribed winds, surface salinity and surface temperature fields. In experiments carried out with such models, ocean ventilation and oxygen concentrations are, not surprisingly, heavily dependent on the characteristics of the forcing applied at the surface. In their Late Permian simulations, *Hotinski et al.* [2001] obtained well ventilated bottom conditions when experiments were forced with a strong equator-to-pole temperature gradient (~28°C) and widespread bottom anoxia in the experiments forced with a weak equator-to-pole gradient (~12°C). When forced with fluxes from a Late Permian atmospheric model, the uncoupled ocean model adopted by *Zhang et al.* [2001] produced a stable, well ventilated "thermal mode" with sinking at high latitudes and high oxygen concentrations near the bottom. By arbitrarily increasing the hydrological cycle to twice the present-day and decreasing the vertical mixing by 40%, the authors obtained a unstable "haline mode," characterized by intermittent sinking at mid latitudes which leads to periodic deep ocean anoxia events lasting about 2800 years [*Zhang et al.*, 2001].

[10] 2. The Earth system model of intermediate complexity is the type of model adopted in this study. The EMICs which have been used to investigate the PTB are based on a 3D ocean model coupled to a 2D energy balance atmospheric model. EMICs are capable of directly simulating a large number of oceanic parameters, such as currents and dissolved O_2, but winds must be prescribed. While winds are not resolved, other atmospheric parameters such as air temperature, moisture and precipitation can be explicitly represented. In some models the land surface characteristics are prescribed while others (like the one used here), contain a dynamic vegetation model which determines land surface cover as a function of climate. The more simple atmosphere component results in fast integration times, allowing the realization of large number of simulations where the sensitivity of results to different boundary conditions, forcings and model parameters can be analyzed.

[11] Previous EMIC PTB simulations with no carbon cycle submodel and prescribed freshwater flux between the ocean and the atmosphere produced generally well oxygenated bottom waters [*Winguth and Maier-Reimer*, 2005]. The exception was a small area of the tropical eastern Panthalassa where O_2 concentrations reached levels below 20 μmol L^{-1}. This deep anoxic area extended up to halfway across equatorial Panthalassa in simulations where an arbitrary 2 sverdrups (10^6 m^3s^{-1}, Sv) freshwater flux was added in southeast Panthalassa [*Winguth and Maier-Reimer*, 2005, Figure 7]. *Winguth and Maier-Reimer* [2005] conducted experiments with atmospheric CO_2 concentrations of 1120 parts per million per volume (ppmv), 2240 ppmv and 5040 ppmv. It is interesting to note that, in the absence of the arbitrary freshwater forcing, the simulation with the highest atmospheric CO_2 resulted in the best ventilated bottom with no anoxic areas.

[12] *Meyer and Kump* [2008] used an EMIC with an ocean carbon cycle but no vegetation dynamics to evaluate the impact of ocean nutrient concentration on anoxia. The authors conducted simulations where nutrient concentrations were equivalent to present-day values and simulations where these present-day concentrations were increased up to 10-fold present-day values. No widespread bottom anoxia was produced under the present-day nutrient scenario. The high nutrient experiments resulted in anoxic conditions within the Tethys Sea, but the deep Panthalassa basin remained well oxygenated [*Meyer and Kump*, 2008].

[13] 3. Atmosphere-ocean general circulation models have coupled 3D ocean, 3D atmosphere and sea ice components. We are aware of only one set of published results based on an AOGCM PTB simulation [*Kiehl and Shields*, 2005]. This model was capable of simulating both winds and ocean currents. The winds used to force our EMIC simulations come from the *Kiehl and Shields* [2005] simulation. Exchanges of mass and energy between the land surface and the atmosphere depended on different land cover types which were prescribed by a paleovegetation reconstruction and remained constant during the simulations (vegetation cover influenced climate but was not influenced by climate). The *Kiehl and Shields* [2005] AOGCM did not incorporate a carbon cycle submodel, and since it did not have an ocean biogeochemical component it could not provide dissolved oxygen concentrations. Nevertheless, under CO_2 concentrations of 3550 ppmv, their modeled meridional overturning was weak. Lacking direct oxygen results, the authors use ideal age, the time in years since the water was last at the surface, to estimate deep ocean ventilation. The ideal age of the deep waters in the equatorial Panthalassa and particularly the Tethys Sea are larger than what their model

Table 1. List of Experiments[a]

Experiment	CO_2	Paleography	Bathymetry
1xPD_C_FL	300	closed	flat
1xPD_O_FL	300	open	flat
10xPD_C_FL	3000	closed	flat
10xPD_C_AM	3000	closed	meridional
10xPD_C_BG	3000	closed	realistic
10xPD_O_FL	3000	open	flat
10xPD_O_AM	3000	open	meridional
10xPD_O_BG	3000	open	realistic
15xPD_O_FL	4500	open	flat

[a]CO_2 is atmospheric concentration in ppmv. "Open" and "closed" refer to the land connection between Angara and Euroamerica. "Realistic" refers to the best guess realistic distribution of oceanic ridges. See Figure 1.

produces for the present-day climate, an indication that their model could produce deep anoxic conditions in the PTB [*Kiehl and Shields*, 2005, Figure 4].

[14] Independent of model complexity, all of these earlier PTB simulations adopted a single paleogeography configuration and flat ocean bottom topography [*Hotinski et al.*, 2001; *Winguth et al.*, 2002; *Winguth and Maier-Reimer*, 2005; *Kiehl and Shields*, 2005; *Meyer et al.*, 2008]. Our experiments, as far as we know, are the first to address the response of modeled PTB ocean circulation and oxygen levels to different bottom topographies and paleogeographic configurations. Our simulations are also the first to directly evaluate ocean PTB acidity through the use of a coupled climate-carbon cycle model.

2. Model Description

[15] The University of Victoria Earth System Climate Model (UVic ESCM) is an EMIC which has been extensively used in previous studies of present day and past climate, including the Last Glacial Maximum and the Ordovician [*Weaver et al.*, 2001; *Schmittner et al.*, 2002; *Poussart et al.*, 1999]. It consists of a vertically integrated energy-moisture balance atmospheric model coupled to version 2.2 of the Geophysical Fluid Dynamics Laboratory Modular Ocean Model [*Pacanowski*, 1996] and a dynamic-thermodynamic sea-ice model. The terrestrial carbon model is based on two components, a modified version of the MOSES2 land surface model and the TRIFFID dynamic vegetation model [*Meissner et al.*, 2003; *Matthews et al.*, 2004]. TRIFFID defines the state of the terrestrial biosphere in terms of soil carbon, and the structure and coverage of five plant functional types (PFTs), broadleaf tree, needleleaf tree, C3 grass, C4 grass and shrub [*Cox*, 2001]. Growth of each PFT is based on a photosynthesis-stomatal conductance model with photosynthetic rates and stomatal resistances dependent on both climate and atmospheric CO_2 concentrations.

[16] Ocean carbon is simulated by an Ocean Carbon-Cycle Model Intercomparison Project type inorganic carbon cycle model and a nutrient-phytoplankton-zooplankton-detritus marine ecosystem model [*Schmittner et al.*, 2008; *Eby et al.*, 2009]. The model does not address the long term (millions of years) component of the carbon cycle. Processes such as Ca-Mg silicate weathering and the burial and subduction of organic carbon and calcium carbonate are not simulated. This constraint would make the model unsuitable for simulations of the ultimate recovery from the PTB.

[17] Water, energy and carbon are conserved without flux adjustments. Freshwater fluxes are calculated by the model and not prescribed, as in some previous PTB EMICs [*Winguth et al.*, 2002; *Winguth and Maier-Reimer*, 2005]. All components of the model have horizontal resolution of 1.8° × 3.6°. The adopted version of the ocean model has 15 vertical levels with grid box thickness varying from 50 m at the surface to about 500 m near the bottom.

[18] Earth at the PTB time resided in a supercontinental configuration with a single continent, Pangea, surrounded by a single Panthalassan ocean. A major oceanic embayment, Tethys, characterized central-east Pangea, and opened to the east into western Panthalassa. Permian-Triassic base continental configuration, topography and winds were provided by the Late Permian AOGCM climate model simulation described by *Kiehl and Shields* [2005]. Experiments are conducted under present-day insolation and orbital parameters, including day length. Atmospheric albedo and atmospheric diffusion are zonal averages of present-day values. No land glaciers are represented. Maximum ocean depth is set to 4000 m. Calcifying plankton, which did not exist during the Permian, are excluded from the ocean biology submodel.

[19] The large differences between present-day and Late Permian vegetation make modeling the land surface for the period challenging. Previous efforts have opted for fixed land surface conditions which were either set to bare soil [*Winguth et al.*, 2002; *Winguth and Maier-Reimer*, 2005], uniform savanna [*Gibbs et al.*, 2002; *Rees et al.*, 1999, 2002], or fixed vegetation based on paleo-reconstructions [*Kiehl and Shields*, 2005]. While we are aware that the five PFTs present in TRIFFID do not provide a perfect representation of Permian flora, we believe that our modeled vegetation is useful as a biome indicator, and opt to incorporate the dynamical vegetation model in our simulations in order to compare our results with biome reconstructions for the period [*Rees et al.*, 2002].

3. Experiments

[20] Nine experiments are conducted to evaluate how changes in atmospheric greenhouse gas concentration (expressed in terms of CO_2 equivalent), ocean bathymetry and paleogeography influence modeled climate and biogeochemistry (Table 1). Simulations are conducted under three atmospheric CO_2 concentrations: 300 parts per million per volume (ppmv), 3000 ppmv and 4500 ppmv. The lower bound is close to present-day concentrations with the two upper values being contained within the uncertainty of CO_2 reconstructions for the period [*Berner and Zavareth*, 2001; *Kidder and Worsley*, 2004]. The 300, 3000 and 4500 ppmv simulations are labeled 1xPD, 10xPD and 15xPD respectively.

[21] While some paleogeographic reconstructions have Angara and Euroamerica joined at the PTB [*Stampfli and Borel*, 2002; *Sengör et al.*, 1993], other reconstructions point to an open gateway [*Blakey*, 2003] between these landmasses during this time. To evaluate the impact of paleogeographic uncertainty on results experiments are performed for two continental configurations: open (O) or closed (C) ocean gateway between Angara and Euroamerica. Also tested is the sensitivity to three ocean bathymetry configurations: flat bottom (FL), arbitrary meridional ridges

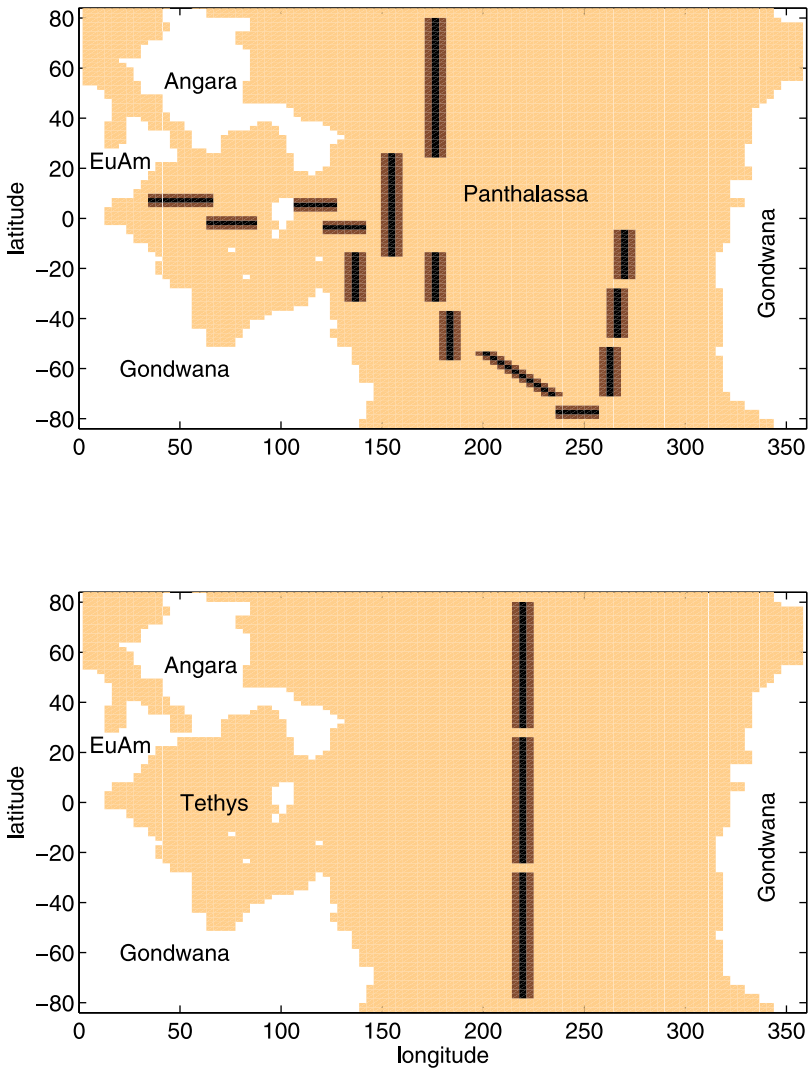

Figure 1. Sensitivity to paleogeography and bathymetry. (top) Example of open Euroamerica-Angara connection with realistic ridge configuration; (bottom) example of closed Euroamerica-Angara connection with meridional ridge configuration.

(AM) and best guess estimate of realistic ridge distribution (BG). Ridges for AM and BG experiments are represented by a two step decrease in depth with ridge crest bins at 2600 m and adjoining bins at 3000 m depth (Figure 1). The nonridge areas of the AM and BG simulations and the whole ocean bottom in the FL experiments have a fixed depth of 4000 m.

[22] The BG distribution of mid-ocean ridges is speculative. Mid-ocean ridges are passive features and cannot be tied directly to mantle convection cells. Nonetheless, geodynamic models [*Collins*, 2003] were used to broadly constrain areas of mantle upwelling and it is assumed that some regions were more likely to have been characterized by mid-ocean ridges. Our understanding of paleogeographic evolution across the period provides clues as to plate motions and the location of plate boundaries, including mid-ocean ridges [*Stampfli and Borel*, 2002], and were used to further constrain the likely locations of ridges. Fault bound rock sequences (terranes) of Upper Carboniferous to Lower Permian age that originated within or adjacent to the Tethyan Sea, including decapitated seamounts, have been documented in the Cordilleran orogens of the northern and southern Americas. These exotic terranes began to accrete to the Americas in the Triassic, and their translation from the Tethyan region east across Panthalassa to the Cordilleran margin requires subduction of the oceanic lithosphere that lay east of the terranes and growth of oceanic lithosphere behind them to the west [*Johnston and Borel*, 2007]. At least one north-south-oriented, eastward-migrating mid-ocean ridge (and more likely two) is required to facilitate the Upper Permian to Triassic eastward translation of terranes across Panthalassa. Beginning in the middle Permian, a ribbon continent of Gondwanan affinity drifted north across the Tethyan sea, separating a northern Paleotethys from a southerly Neotethys, and requiring the presence of an east-west trending Tethyan mid-ocean ridge located behind (south of) the northward drifting ribbon [*Sengör*, 1984]. As with modern ridges, it is assumed that ridges are character-

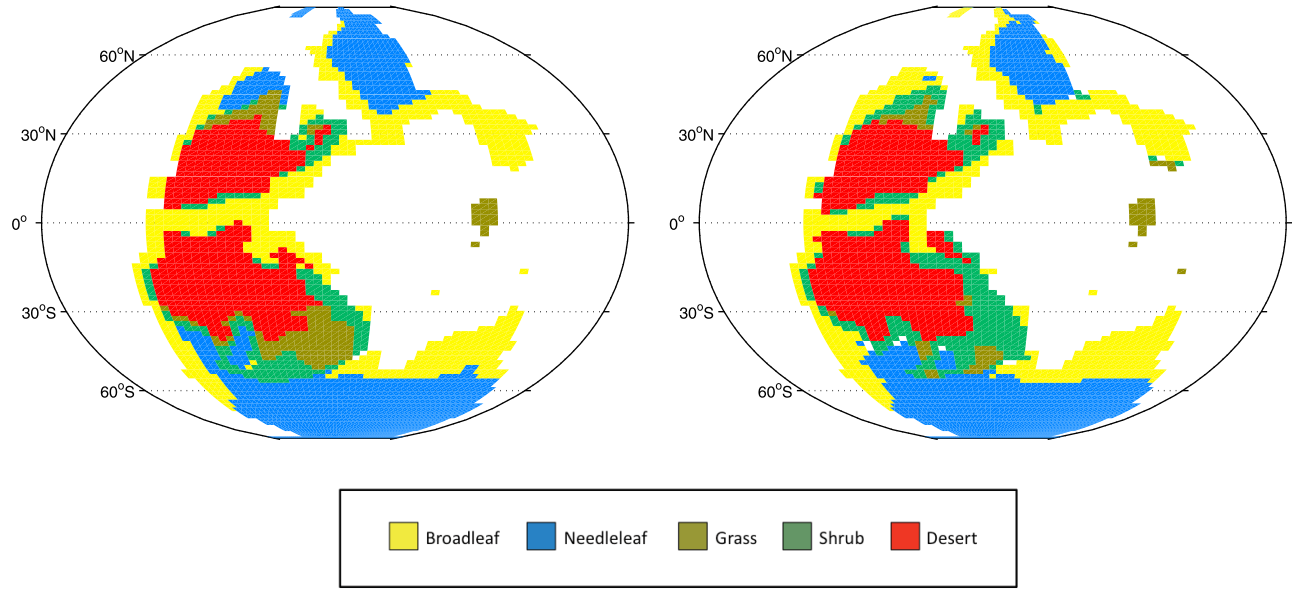

Figure 2. Dominant plant functional type. (left) 10xPD_C_FL; (right) 15xPD_O_FL.

ized by segments that are bound by transform faults, that the ridge segments step in a consistent direction, and that the offsets along the transform faults are generally minor and do not fully disrupt the topographic high that characterizes the ridge axis. Ridge sections are oriented such that implied plate motions are consistent with rotations about Euler poles.

[23] Simulations are initialized with present-day zonal mean atmospheric temperature and moisture, zonal means for ocean temperature and salinity and a vegetation free surface. Experiments are integrated until equilibrium. The length in model years until equilibrium is reached was experiment dependent, so that simulation length varied from about 8,000 to 12,000 model years. Equilibrium is assumed when modeled global millennial trends are at or below the following values: for ocean temperature, 5 10^{-3}°C; for ocean dissolved inorganic carbon, 3.30 10^{-4} mol m^{-3} and for ocean dissolved oxygen, 4.35 10^{-1} μmol m^{-3}.

4. Results and Discussion

[24] We start by comparing our modeled precipitation-evaporation (P-E) and vegetation results to climate sensitive experiments and biome reconstructions for the period. We then present our modeled surface temperature, meridional overturning circulation (MOC), ocean oxygen and surface ocean carbonate chemistry results. Whenever possible, results are discussed in the light of reconstructions and previously published simulations.

4.1. Precipitation-Evaporation and Vegetation Cover

[25] There is good agreement between modeled vegetation cover (Figure 2) and middle-to-Late Permian biomes as reconstructed by *Rees et al.* [2002] (Figure 3). While differences in land cover categories do no allow direct comparisons, the simulations generate desert and vegetation associated with arid climates (grass and shrub) in most areas defined as desert by the *Rees et al.* [2002] reconstruction. There is also good agreement between the midlatitude to high-latitude areas covered by needleleaf trees in the model and areas occupied by reconstructed cool temperate and cold temperate biomes. The same can be said for the continental equatorial region, where modeled broadleaf tree distribution

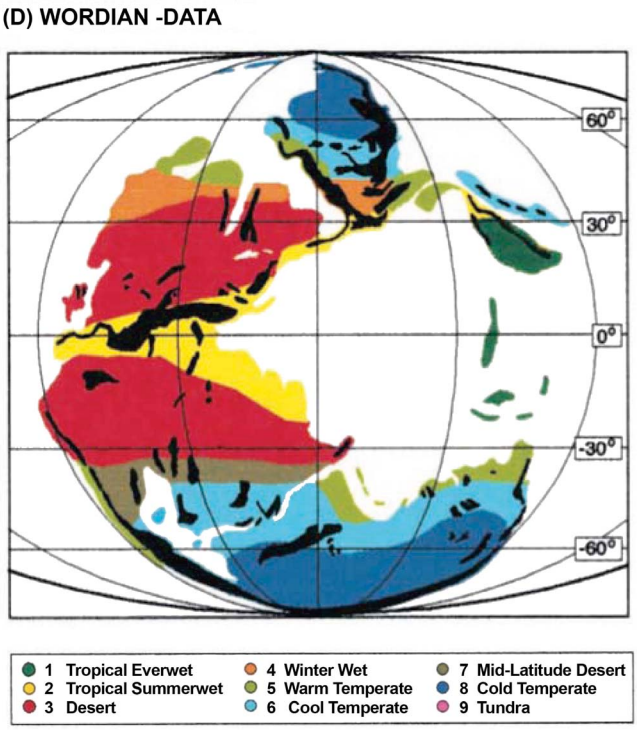

Figure 3. Data-derived middle-to-Late Permian biome reconstruction from *Rees et al.* [2002]. Reproduced here with permission from the University of Chicago Press, all rights reserved.

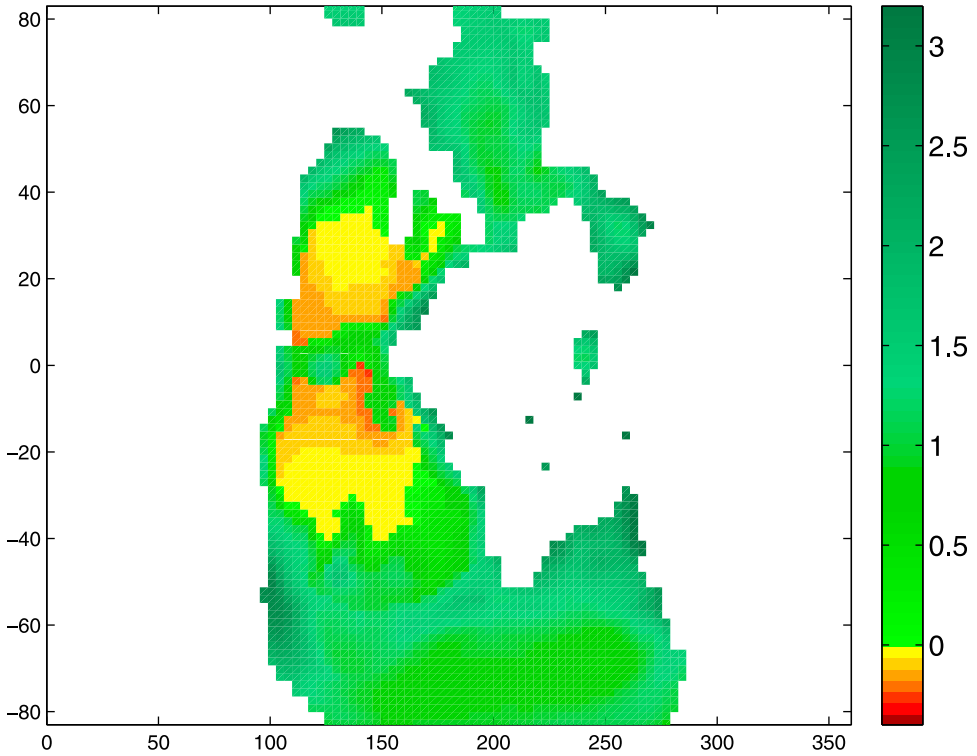

Figure 4. Annual mean precipitation minus evaporation in 10^{-5} kg m^{-2} s^{-1} for the 10xPD_C_FL.

matches the tropical summer wet biome and for the mid latitudes in the east coast where tropical ever wet (in the north) and warm temperate (in the south) reconstructed biomes occur over areas where the simulations generate broadleaf trees. The simulations produce broadleaf coverage in a band along the southern hemisphere west coast occupied by the warm temperate biome. A mismatch occurs along the low latitude west coast, where the model produces broadleaf trees and the *Rees et al.* [2002] reconstruction points to desert conditions. The NW corner of Euroamerica is occupied by broadleaf trees for the 15xPD simulation, which is in better agreement with the warm temperate and winter wet reconstructed biomes than the 10xPD experiments which produce needleleaf coverage in this area.

[26] The simulated areas of negative P-E (Figure 4) compare well with the observed distribution of evaporites for the Wordian (~266 Ma, middle Permian), which are found in the western portions of continental Euromerica and Gondwana poleward of 20° in both hemispheres [*Ziegler et al.*, 1988] by *Rees et al.* [2002]. The same study of climate sensitive sediments points to the presence of coal in the interior and west coast of the middle to high latitudes, which are areas of positive P-E in our simulations. The only clear disagreement between our model and the *Ziegler et al.* [1988] sediment analysis occurs at the eastern Gondwana coast between 20°S and 30°S. This is an area of positive modeled P-E where, according to the *Ziegler et al.* [1988] results, evaporites are abundant. Lack of PTB observations required us to compare Wordian sediments to our modeled P-E. There is evidence that, at least at continental to regional spatial scales, the relative abundance of plant genera did not change drastically between the Middle and Late Permian [*Rees*, 2002]. While this by itself cannot be used as proof that global climate did not vary significantly between the two periods, it does offer some support to the possibility that this might have been the case.

4.2. Surface Temperature

[27] In agreement with paleoproxy data, modeled PTB surface ocean and air temperatures are markedly higher than at present day [*Kidder and Worsley*, 2004; *Erwin*, 1994] (Figure 5). The spatial distribution of surface temperatures produced by our simulations is also in general good agreement with modeling studies which, like ours, adopt a 3D ocean model [*Winguth et al.*, 2002; *Winguth and Maier-Reimer*, 2005; *Kiehl and Shields*, 2005]. It should be noted that, particularly at low latitudes, our annual mean surface temperatures tend to be 2°–4° warmer than these previous simulations [*Winguth et al.*, 2002; *Winguth and Maier-Reimer*, 2005; *Kiehl and Shields*, 2005]. In the case of the *Winguth et al.* [2002] and *Winguth and Maier-Reimer* [2005] results, this difference might be at least partially related to the fact that our experiments are forced with present-day insolation while these authors adopted an insolation value which is 2.1% smaller than present day.

[28] The high CO_2 simulations show low ocean surface temperatures (from 2° to 4°C) in the SW corner of Panthalassa, adjacent to the landmass that is now eastern Australia. The lowest mean annual land surface temperatures for the whole globe, with values reaching −5°C, are found in the area adjacent to these cold waters, in SE Gondwana (Figure 5). This local temperature minimum can also be noted by the pattern in snow thickness over land and the presence of sea ice in the area (Figure 6). This is in agreement with the

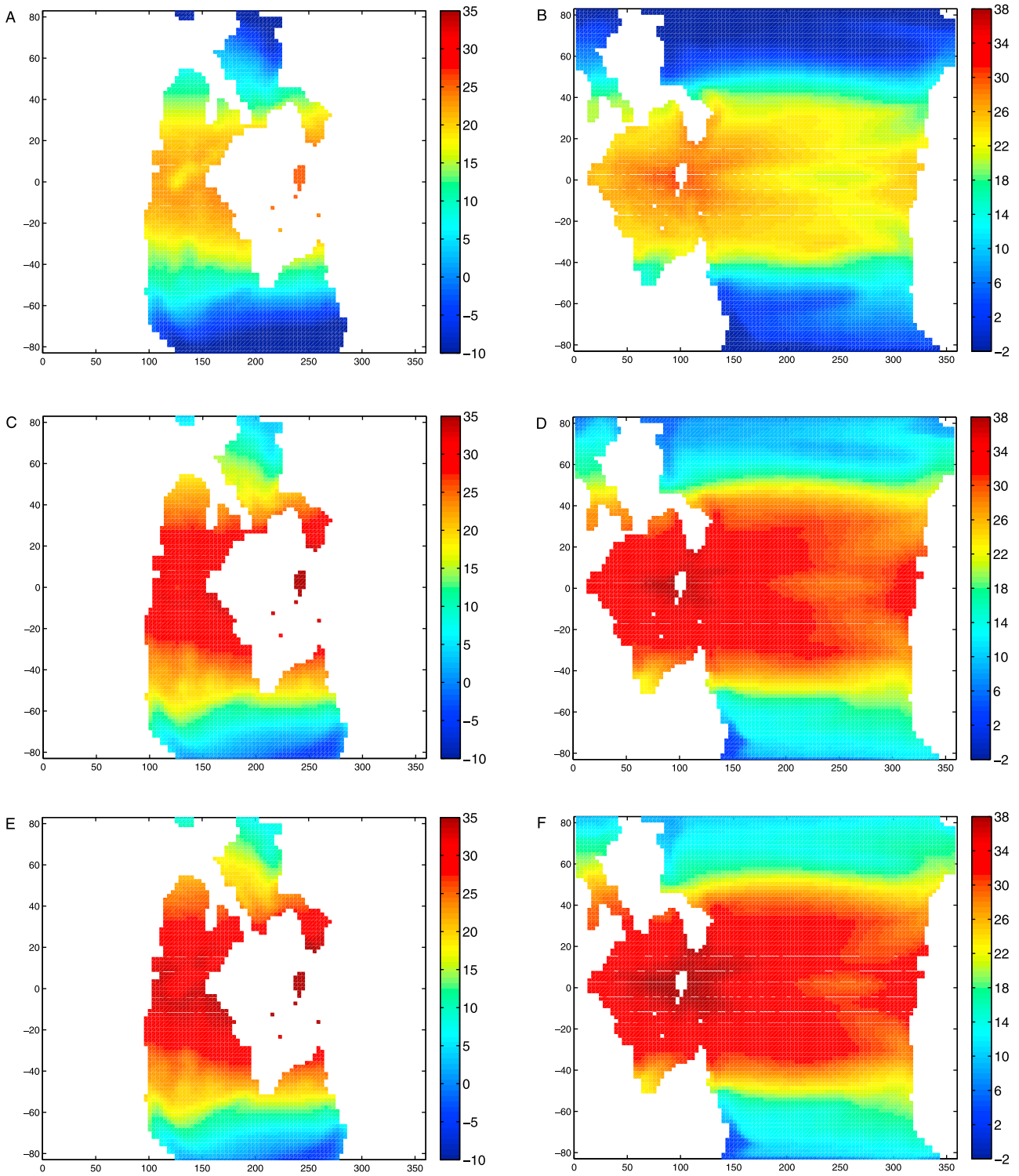

Figure 5. (left) Annual mean surface air and (right) annual mean surface ocean temperatures in degrees Celsius; (a and b) 1xPD_C_FL, (c and d) 10xPD_C_FL, and (e and f)15xPD_O_FL. Note shift in the longitude axis between land and ocean images. Key to experiments provided in Table 1.

interpretation of the geological record which indicates the presence of cold climatic conditions over eastern Australia late into the Permian, with western Australia being warmer than the east during this period [*Jones et al.*, 2006]. Coastal upwelling has been proposed as an explanation for both the cold ocean climate and the east-to-west temperature gradient in the region [*Jones et al.*, 2006]. In our simulations however, these cold surface waters are not a result of upwelling but are associated with the formation of a low salinity lens at the surface. This layer cools due to contact with the atmosphere

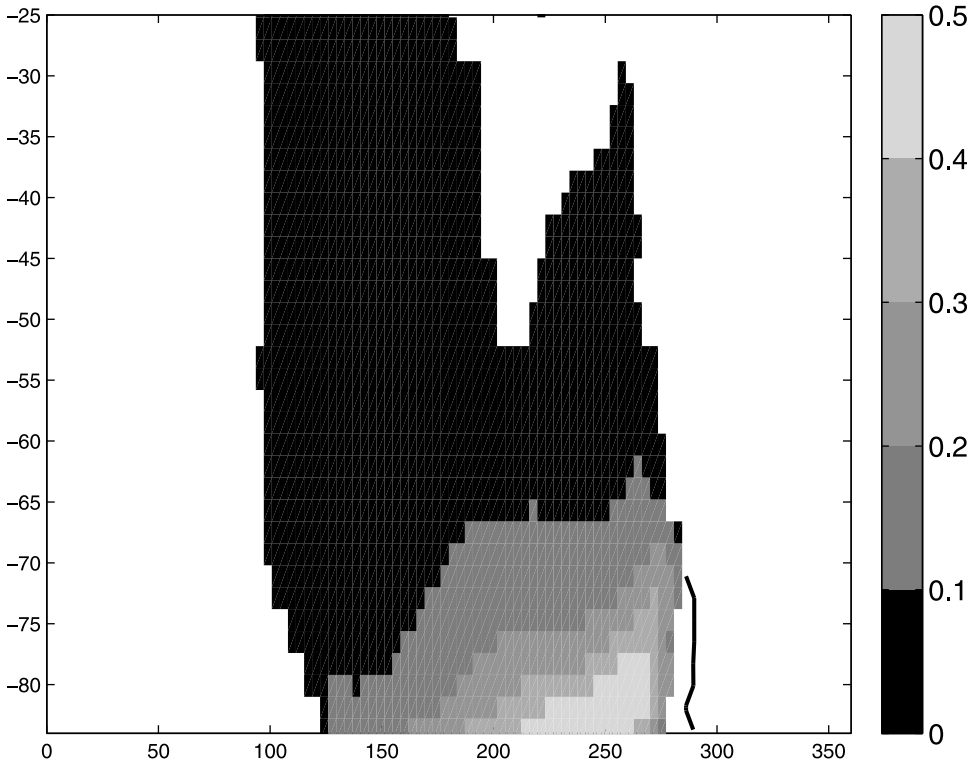

Figure 6. Annual mean snow thickness in meters and maximum sea-ice extent (black line) for the 10xPD_C_FL experiment.

and remains cold because, given its larger buoyancy, it does not mix with lower layers (Figure 7). The low temperatures in the area are restricted to the model top layer and temperatures increase rapidly with depth (not shown). Our modeled ocean and land surface temperature in the SW corner of Panthalassa and SE Gondwana are consistent with the temperature distribution generated by the fully coupled *Kiehl and Shields* [2005] simulation but are not in agreement with previous EMIC simulations which showed warmer temperatures in coastal regions compared to cold temperatures in the center of Gondwana at high southern latitudes [*Winguth et al.*, 2002; *Winguth and Maier-Reimer*, 2005].

[29] The accumulation of chert along the northwest margin of Euroamerica from about 280 Ma up to, but not after, the PTB is seen as evidence for cold oceanic conditions and the presence of sea ice in the region during the period [*Beauchamp and Baud*, 2002]. The absence of chert at the PTB has been interpreted as the result of increasing temperatures and of the slowing down of the MOC [*Beauchamp and Baud*, 2002]. In agreement with these findings, no sea ice is found in the northern hemisphere for high CO_2 experiments. Sea ice is formed in the northern hemisphere during the 1xPD_C_F simulation, reaching a maximum equatorward position of 50°N in the western Panthalassa but the simulation does not produce any sea ice along Euroamerica's northwest margin (not shown).

[30] Large tropical areas of the high CO_2 simulations are occupied by surface waters with temperatures above 30°C, which is the upper limit of temperature tolerance of many present-day oceanic animals, particularly invertebrates [*Clarke*, 1993]. Our results indicate that temperature could also have acted as a stressor on oceanic life during the PTB.

4.3. Meridional Overturning Circulation

[31] The modeled MOC is discussed in light of its relevance to deep ocean oxygen concentrations. From this perspective the main result is that, for all experiments, the intensity of overturning circulation indicate generally well-ventilated deep and bottom conditions (Figures 8 and 9). The warmer temperatures of the high CO_2 simulations did not generate an stagnant ocean. In some cases, and in agreement with previous EMIC results [*Winguth and Maier-Reimer*, 2005], an increase in CO_2 caused an increase in modeled MOC transport (differences between Figures 8a and 8c).

[32] Our overturning values are not consistent with a series of studies which have suggested that many features preserved in the geological record of the Late Permian and the PTB could be explained by a reduction in the MOC during these periods [see, e.g., *Beauchamp and Baud*, 2002; *Wignall*, 2007; *Wignall et al.*, 2010; *Bond and Wignall*, 2010; *Kakuwa*, 2008]. The AOGCM climate simulation by *Kiehl and Shields* [2005] produced a weaker MOC than the one generated by our model. In the *Kiehl and Shields* [2005] simulation, maximum MOC transport between 3000 m and 1000 m varies from about 10 Sv to 5 Sv. In our experiment that best matches the AOGCM results (10xPC_C_FL), the same parameter ranges from about 15 Sv to 30 Sv (Figure 8). Other EMIC simulations have obtained deep MOC transports that are comparable (20 Sv to 25 Sv [*Meyer et al.*, 2008]) or significantly larger (30 Sv

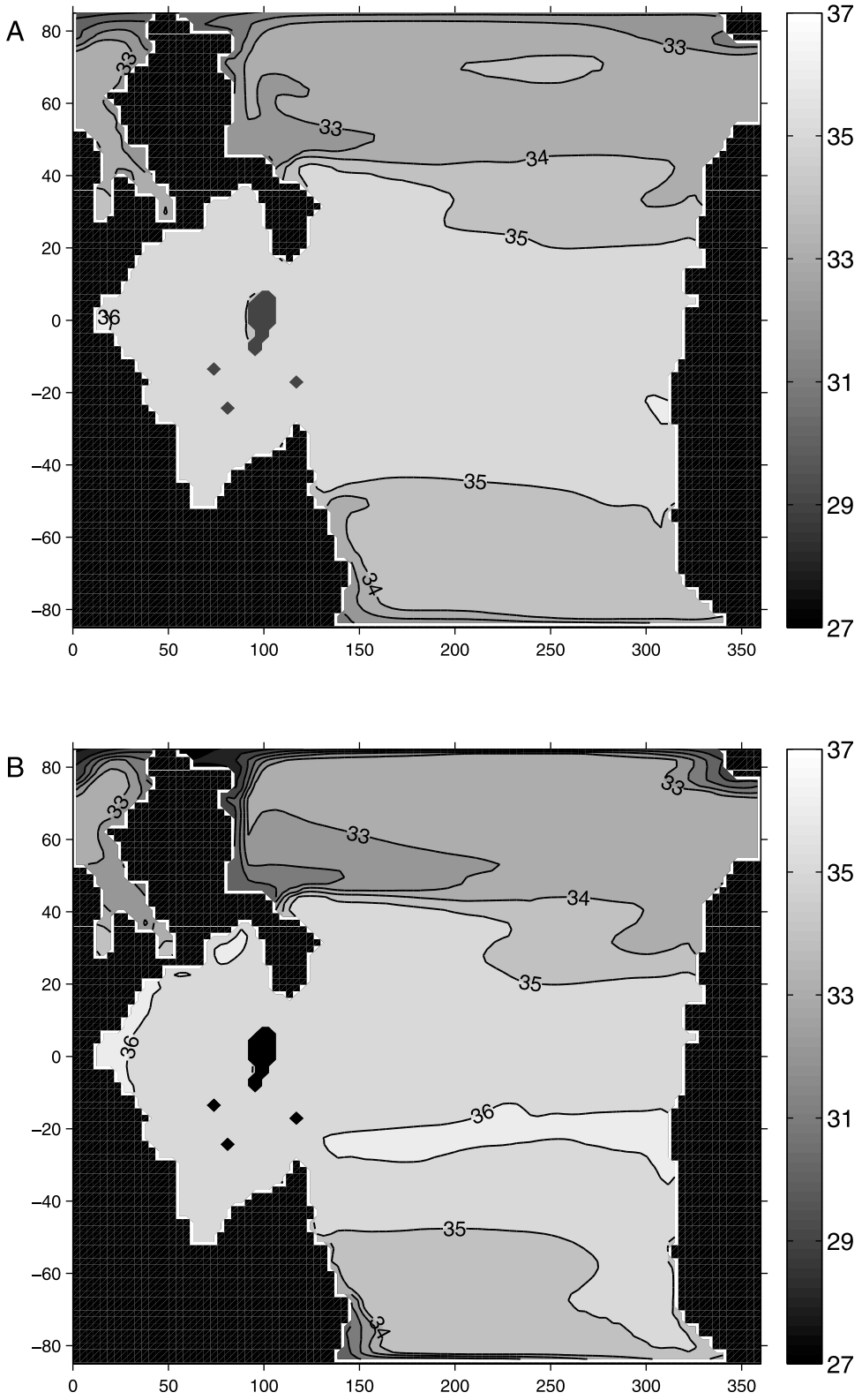

Figure 7. Annual mean ocean surface salinity in PSU: (a) 1xPD_C_FL and (b) 10xPD_C_FL.

to 60 Sv [*Winguth and Maier-Reimer*, 2005; *Winguth et al.*, 2002]) than our results.

[33] The equator-to-pole surface density difference is an important determinant of MOC transport [*Manabe and Bryan*, 1985]. Previous simulations have shown that this difference does not always decrease under high-CO_2 conditions, meaning that MOC transport is not necessarily reduced under warmer climates [*Manabe and Bryan*, 1985].

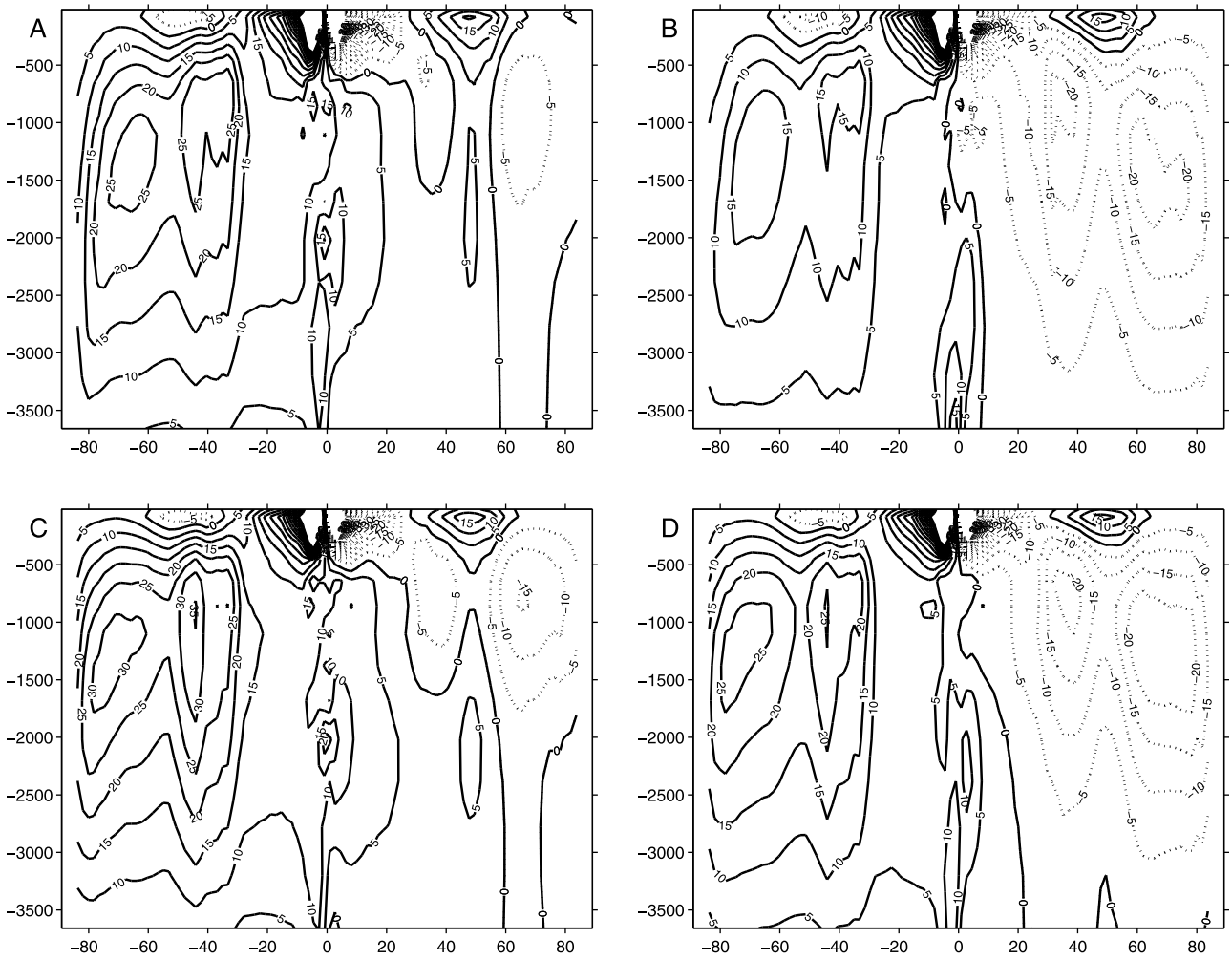

Figure 8. Annual mean meridional overturning circulation transport (Sv) for flat bottom simulations: (a) 1xPD_C_FL, (b) 1xPD_O_FL, (c) 10xPD_C_FL, and (d) 10xPD_O_FL.

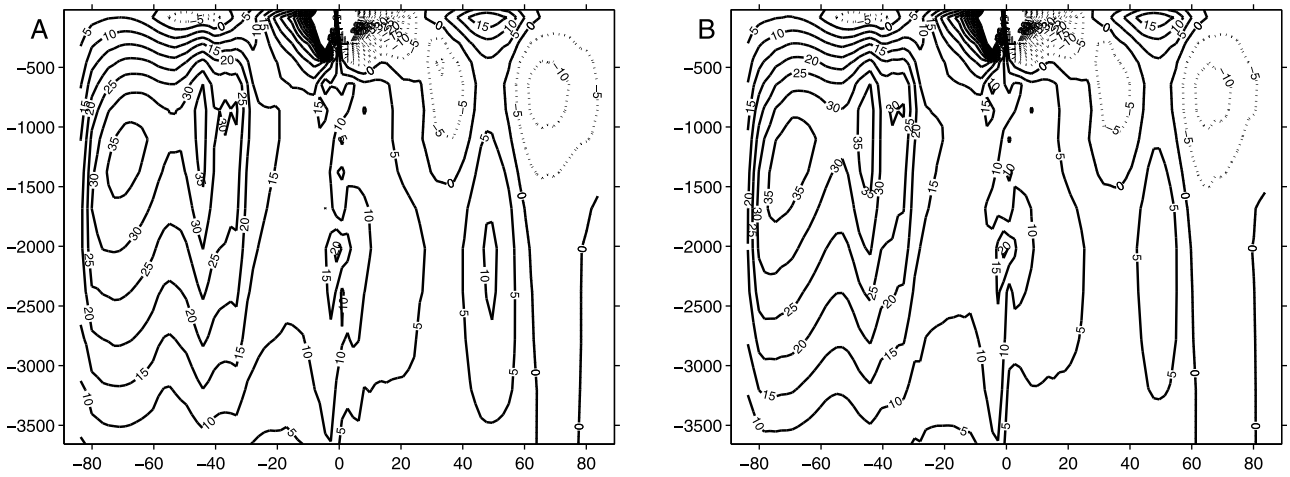

Figure 9. Annual mean meridional overturning circulation transport (Sv) for two ridge configurations at 10xPD CO_2. (a) Closed gateway, best guess (10xPD_C_BG); (b) closed gateway, meridional (10xPD_C_AM).

Table 2. Difference in Mean Annual Surface Water Density, ρ, and Temperature, T, Between the Equatorial Region and the High Southern and High Northern Latitudes for Different Atmospheric CO_2 Concentrations[a]

Parameter	High Southern ρ (kg m^{-3})	High Northern ρ (kg m^{-3})	High Southern T (°C)	High Northern T (°C)
1xPD	3.75	3.34	−23.59	−24.50
10xPD	4.92	4.37	−22.01	−22.41
15xPD	5.06	4.76	−22.26	−21.12

[a]Equatorial region, ±7°; high southern latitude, area below −75°; high northern latitude, area above 75°. With the exception of the 15xPD case, for which only open gateway values exist, the differences represent the average of the flat bottom open and flat bottom closed gateway experiments.

In our experiments, while the equator-to-pole surface temperature gradient tends to be lower under higher CO_2, the equator-to-pole surface density gradient actually increases (Table 2), a result which is in accordance the simulations reported by *Manabe and Bryan* [1985] and help explain the larger MOC values of our high CO_2 experiments.

[34] For both our closed and open configurations, the presence of mid-ocean ridges produces a stronger southern cell with a small weakening and shoaling of the northern cell. The result is an increase in the asymmetry of the cells and also in the maximum deep overturning transport. In the case of the closed gateway experiments, for example, the presence of ridges increases the maximum deep overturning transport by about 15% to 20%. The MOC of different ridge arrangements under the same gateway configuration are very similar (Figure 9).

[35] The strength and spatial pattern of the MOC is influenced by the opening or closing of the Angara-Euroamerica gateway. In the high CO_2 simulations, the MOC of the closed configuration is asymmetric in relation to the equator, with a strong southern cell and a weak and shallow northern hemisphere cell. The same asymmetric overturning pattern is seen in some previous EMICs [*Winguth and Maier-Reimer*, 2005; *Winguth et al.*, 2002] but the northern and southern cells of the *Meyer et al.* [2008] EMIC and

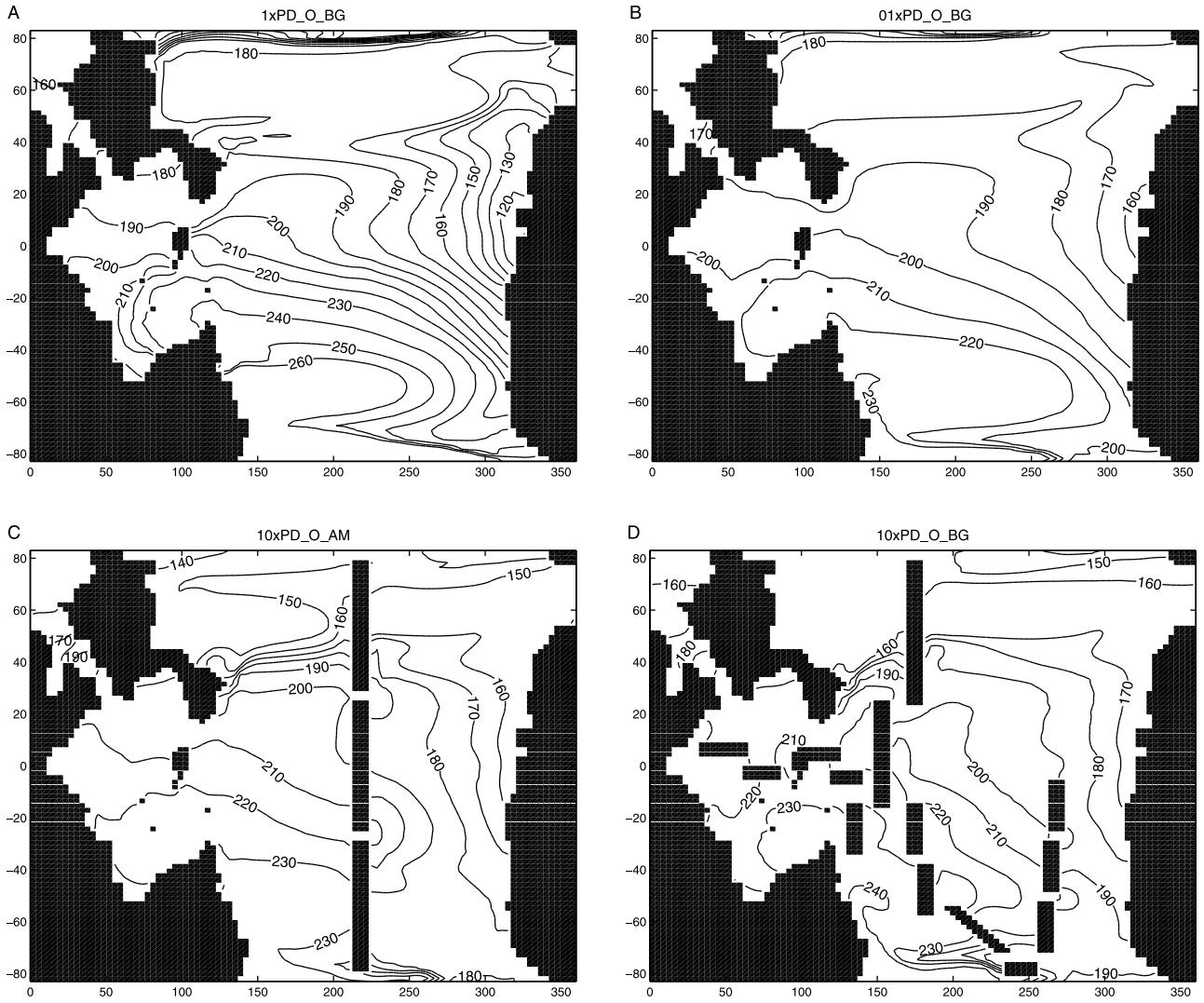

Figure 10. Annual mean bottom dissolved oxygen (μmol L^{-1}) for the open gateway configuration: (a) 1xPD_O_FL, (b) 10xPD_O_FL, (c) 10xPD_O_AM, and (d) 10xPD_O_BG.

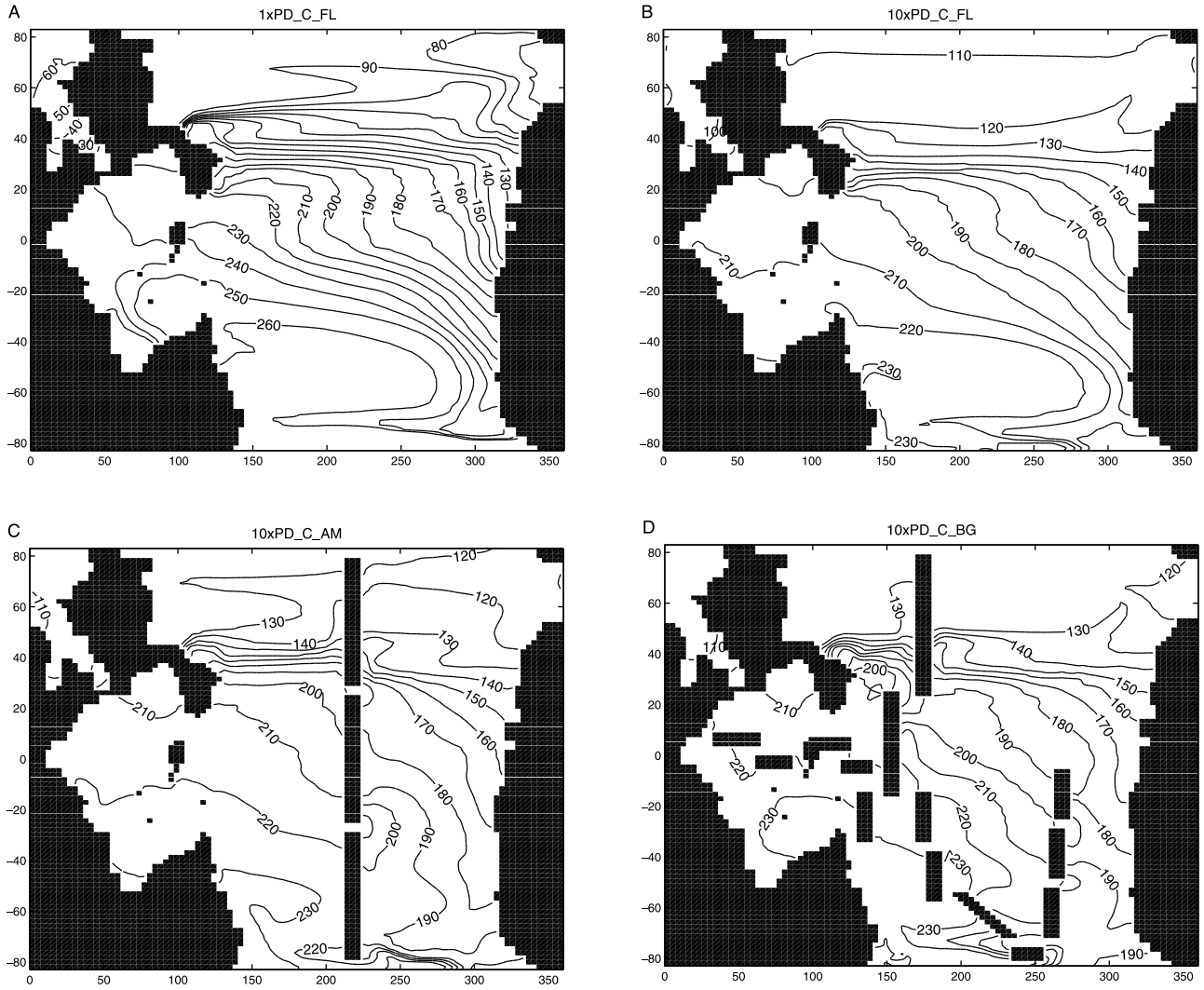

Figure 11. Annual mean bottom dissolved oxygen (μmol L^{-1}) for the closed gateway configuration: (a) 1xPD_C_FL, (b) 10xPD_C_FL, (c) 10xPD_C_AM, and (d) 10xPD_C_BG.

the *Kiehl and Shields* [2005] AOGCM MOC transport are of similar strength.

4.4. Ocean Oxygen Concentrations

[36] None of the nine model configurations produce generalized deep ocean anoxia (Figures 10 and 11). The distribution of deep O_2 in the 15xPD_O_FL (not shown) is similar to the 10xPD flat bottom results. The presence of ridges and their distribution alter the spatial pattern of deep oxygen concentrations, with lower values in eastern Panthalassa for simulations where ridges are present. The 1xPD CO_2, closed gateway experiment shows anoxic bottom waters in the narrow sea between Angara and Euroamerica. An oxygen minimum, with values between 80 μmol L^{-1} and 100 μmol L^{-1} is found in the same area of the closed gateway high CO_2 simulations (Figures 11b–11d).

[37] Previous EMIC simulations with fixed freshwater flux, flat-bottom bathymetry and atmospheric CO_2 ranging from 4xPD to 8xPD produced low (<20 μmol L^{-1}) oxygen concentrations in a small area of the tropical eastern Panthalassa [*Winguth and Maier-Reimer*, 2005]. This deep anoxic area extended up to halfway across equatorial Panthalassa in simulations where an arbitrary 2 Sv freshwater flux was added in southeast Panthalassa [*Winguth and Maier-Reimer*, 2005, Figure 7]. While our experiments show tropical eastern Panthalassa being occupied by anoxic waters at middepth, these low oxygen levels do not extend to the bottom waters (Figure 12). This configuration of anoxic middepth and well ventilated bottom is similar to what is observed in the present-day eastern tropical Pacific [*Garcia et al.*, 2006].

[38] A well-oxygenated bottom was also obtained by *Hotinski et al.* [2001] for simulations with their uncouple ocean model forced with a ~28°C equator-to-pole temperature difference (i.e., their strong gradient experiment). Our simulations, where ocean temperatures were free to vary, produce meridional temperature gradients which are closer to the *Hotinski et al.* [2001] strong equator-to-pole case, with our differences varying from ~24°C for the 1xPD experiments to ~22.5°C for the simulations with higher CO_2 concentrations.

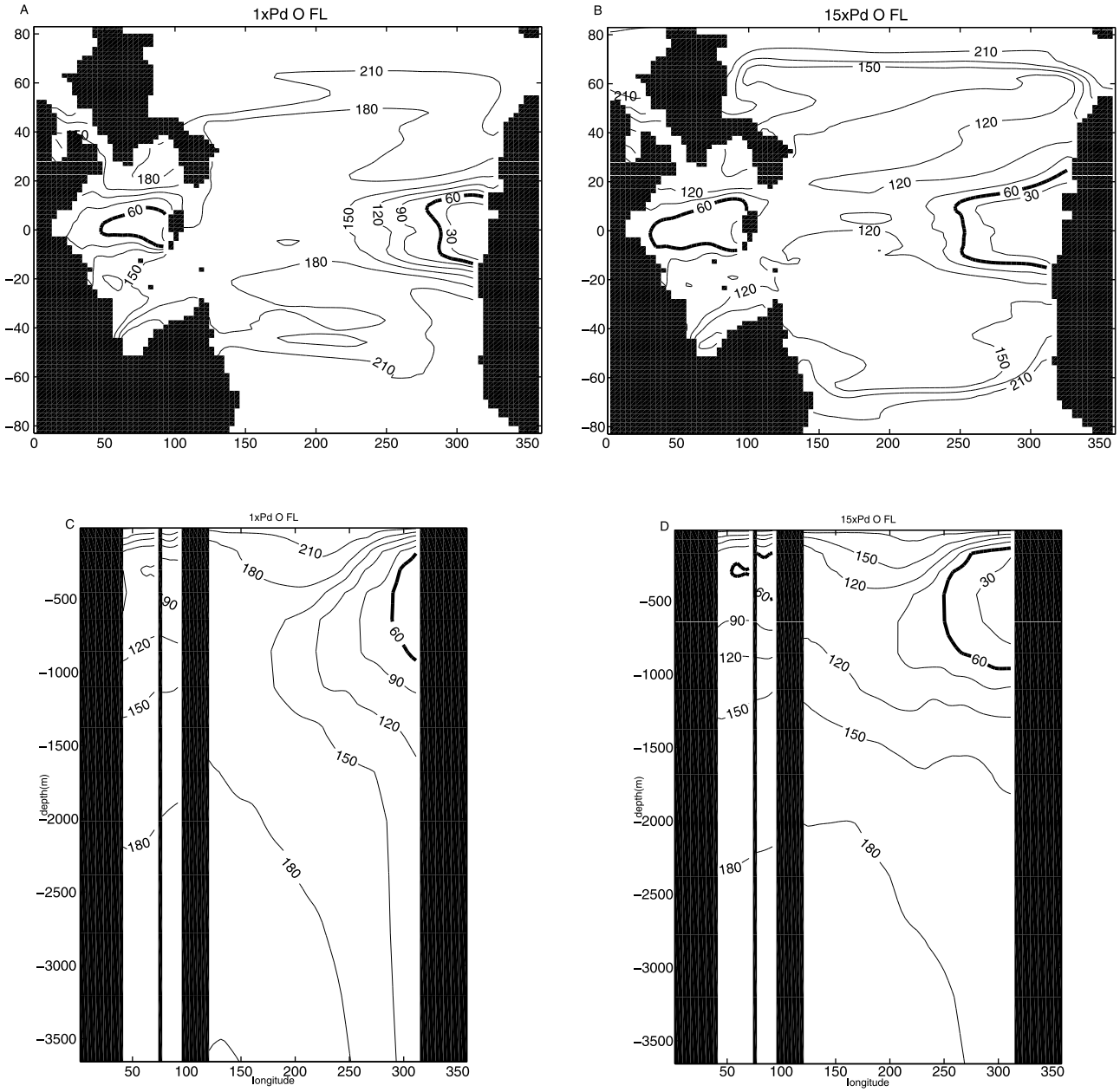

Figure 12. Dissolved oxygen (μmol m L^{-1}). (a) Annual mean values between the depths of 130 m and 980 m for 1xPD_O_FL simulation. (b) Same as Figure 12a for the 15xPD_O_FL. (c) Annual mean values between the latitudes of ±20° for the 1xPD_O_FL simulation. (d) Same as Figure 12c for 15xPD_O_FL. The value of 60 μmol m^{-3}, thick isolines, was selected as the boundary between oxic and anoxic conditions used for the volume calculation (see text).

[39] Our model also generates anoxic conditions (defined here as waters with oxygen concentration at or below 60 μmol L) at middepth in the central Tethys Sea. The increase in CO_2 between the 1xPD and 15xPD simulations results in a doubling of the volume of anoxic middepth waters (Figure 12).

[40] The geological record provides evidence of deep ocean and shelf anoxic conditions during the Late Permian and the PTB [see, e.g., *Wignall and Twitchett*, 1996; *Wignall*, 2007; *Wignall et al.*, 2010; *Bond and Wignall*, 2010]. Geochemical analyses have suggested the existence of generalized deep anoxia for more than 10 million years from the middle-to-Late Permian (~259 Ma B.P.) to the early Triassic [*Kato et al.*, 2002], with some pointing to anoxic conditions reaching the shallow ocean around 2 million years before the PTB and a peak in anoxia at the PTB [*Isozaki*, 1997]. Other studies propose that anoxia was restricted to the latest Permian [*Bond and Wignall*, 2010; *Beauchamp and Baud*, 2002], with some interpretations limiting anoxia to a period of 0.6 to 1.2 million years before the PTB. One of these studies concluded that within this shorter interval, anoxic conditions were punctuated by a series of oxygenation events, including one at the PTB [*Kakuwa*, 2008].

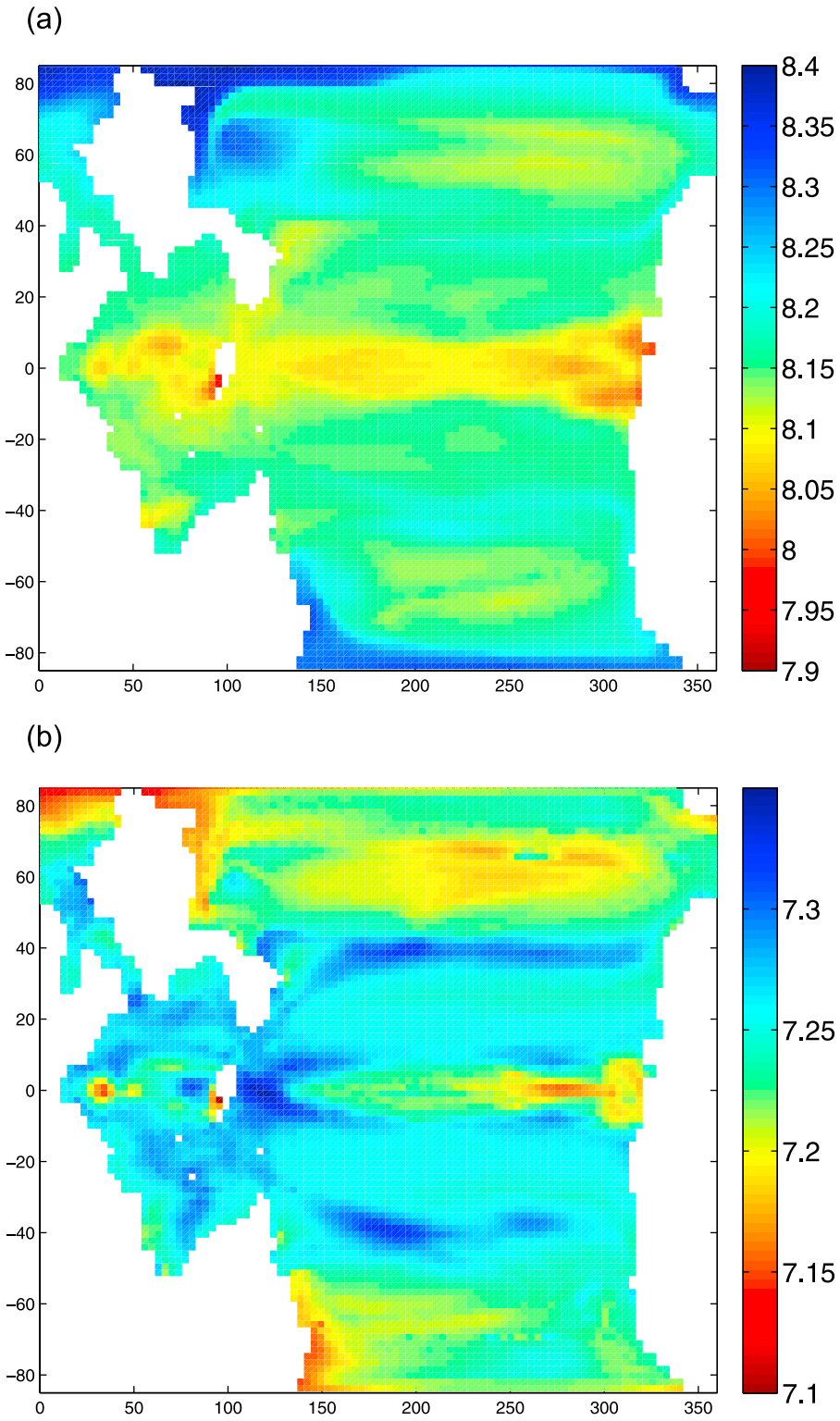

Figure 13. Annual mean ocean surface pH: (a) 1xPD_O_FL and (b) 10xPD_O_FL. Note the differences in color scales.

[41] Several of these observational studies suggest that the inferred anoxic conditions could be explained by global warming, which would have caused a slow-down of the meridional circulation and ocean stagnation [*Wignall*, 2007; *Wignall et al.*, 2010; *Bond and Wignall*, 2010; *Beauchamp and Baud*, 2002; *Kakuwa*, 2008]. Another possible explanation for the anoxia is deep convection of hot, saline and oxygen poor waters at midlatitudes which would then upwell at high latitudes [*Kidder and Worsley*, 2004], similar to the "haline mode" obtained by *Zhang et al.* [2001]. It

should be noted that in the *Zhang et al.* [2001] simulations this mode was unstable, being interrupted every ~2800 years by flushing events that brought well oxygenated water from high latitudes to the bottom. While there was the potential of anoxia being developed, the authors note that the duration of the haline mode circulation was similar to the timescale required for the depletion of oxygen in the deep ocean.

[42] Neither a stagnant ocean nor midlatitude deep convection are reproduced by our simulations and they are also absent from other EMIC modeling efforts [*Winguth and Maier-Reimer*, 2005; *Winguth et al.*, 2002; *Meyer et al.*, 2008]. On the other hand, the weak overturning circulation and long ideal ages in the Tethys and equatorial Panthalassa suggest an stagnant ocean in the *Kiehl and Shields* [2005] AOGCM simulation. It should be noted that, due to differences in spatial resolution and representation of bottom bathymetry, the deep Tethys is significantly more isolated from the Panthalassa in the *Kiehl and Shields* [2005] model than in ours (compare *Kiehl and Shields* [2005, Figure 4] to our Figure 1).

[43] A more sluggish meridional overturning reduces the amount of oxygen delivered to the deep ocean and the upwelling of nutrients to the surface, curtailing primary production. This means that while less oxygen reaches the deep ocean, there is also less export of organic matter from the surface and a decrease in oxygen consumption in this region.

[44] In box model simulations, deep oxygen levels were mostly dependent on nutrient utilization at high latitudes and not on the magnitude of the overturning [*Sarmiento et al.*, 1988]. In uncoupled ocean simulations with vigorous overturning, a doubling in nutrient concentration reduced bottom oxygen levels but did not result in anoxia [*Zhang et al.*, 2001]. More complex numerical simulations with a PTB EMIC (atmospheric CO_2 ~ 10xPD) resulted in two well defined symmetrical overturning cells with transport ranging from 20 to 25 Sv and no deep ocean anoxia under present-day nutrient levels. Even under these well ventilated conditions, anoxia occurs within the Tethys when ocean nutrient concentrations are increased to three to four times above present-day levels [*Meyer et al.*, 2008; *Meyer and Kump*, 2008]. The deep Tethys of the *Meyer et al.* [2008] experiments contain only one small opening into the Panthalassa at 3500 m. This might be one of the reasons why, even in some of their modeled high nutrient scenarios, anoxia is restricted to this basin.

[45] While we do not test the sensitivity of results to changes in nutrient availability and/or rate of nutrient utilization, our results lend support to the argument that the anoxia at the end of the Permian was not caused exclusively by changes ocean dynamics and that biogeochemical processes, like an increase in terrestrial nutrient flux, must have also have played a role.

4.5. Surface Ocean pH and $CaCO_3$ Saturation

[46] For both gateway configurations the increase in atmospheric CO_2 results in a significant reduction of surface ocean pH, with the maximum values of the 10xPD experiments (7.34) being lower than the minimum values of the 1xPD experiments (7.97). The increase in CO_2 also alters surface pH spatial pattern, with the high CO_2 experiments producing a local maximum in the tropical east Panthalassa where the 1xPD simulations show low pH. The 10xPD and 15xPD simulations also show low pH at high-latitude areas where the 1xPD experiments produce low values (Figure 13).

[47] Calcifying organisms precipitate calcium carbonate as aragonite, calcite or high-Mg calcite. For example, modern reef building corals and mollusks tend to form their skeletons and shells from aragonite, calcite is the most common form produced by coccolithophores and foraminifera and many echinoderms and coralline algae precipitate high-Mg calcite [*Kleypas et al.*, 2006]. A decrease in pH is associated with a decrease in carbonate ion concentration and a reduction in the calcium carbonate saturation values. While dissolution of solid calcium carbonate crystals occur only at saturation values below 1.0, calcifying organism can be negatively impacted by a reduction in carbonate ion concentration even if the water remains supersaturated [*Guinotte and Fabry*, 2008]. Under the same physical conditions aragonite and high-Mg calcite are more soluble than calcite.

[48] Present-day reef-forming corals are found in waters with aragonite saturation values ranging from 3.3 to 4.1 with a mean of 3.8 [*Kleypas et al.*, 1999]. Saturation state is not the only parameter controlling calcification in coral reefs which is dependent, among other factors, on temperature [*Reynaud et al.*, 2003]. It has been suggested that the aragonite saturation threshold for coral well-being might lie between 3.2 and 1.3 (J. Kleypas, personal communication, 2008). Many studies have dealt with the impact of increased atmospheric CO_2 on corals in the context of the present anthropogenic emissions [*Kleypas et al.*, 2006]. Simulations indicate that negative effects of temperature increase and acidification promoted by maximum present-day CO_2 emissions, which result in mean atmospheric CO_2 concentrations which are less than half of our 10xPD simulations, would last for at least 10,000 years after emissions stop (K. J. Meissner et al., Multimillennial coral reef habitat recovery: the importance of the terrestrial weathering feedback, submitted to *Global Biogeochemical Cycles*, 2011).

[49] The simulated carbonate ion concentrations of the high CO_2 experiments are analyzed in the context of its potential impact on biota, particularly reef-forming organisms. During the Late Permian, the important reef builders like sponges, phylloid algae and ancestral coralline algae, tended to precipitate the more soluble forms aragonite and high-Mg calcite [*Payne et al.*, 2007; *Stanley*, 2008].

[50] In agreement with the pH results, surface waters of the high CO_2 experiments show significantly lower aragonite and calcite saturation levels than those of the 1xPD simulations (Figures 14 and 15). The maximum aragonite saturation value of the 10xPD simulations is 1.15, which would make the whole surface ocean unsuitable for present-day reef-forming coral species. The maximum aragonite saturation for the 15xPD experiment is 0.77. In the 10xPD simulations, latitudes poleward of ±40° are unsaturated in relation to calcite. The highest calcite saturation state for the 15xPD experiment is 1.12, with values above 1.0 present only over a small area in western equatorial Panthalassa (not shown).

[51] The impacts of anthropogenic CO_2 on ocean carbonate chemistry have already been measured [*Gruber et*

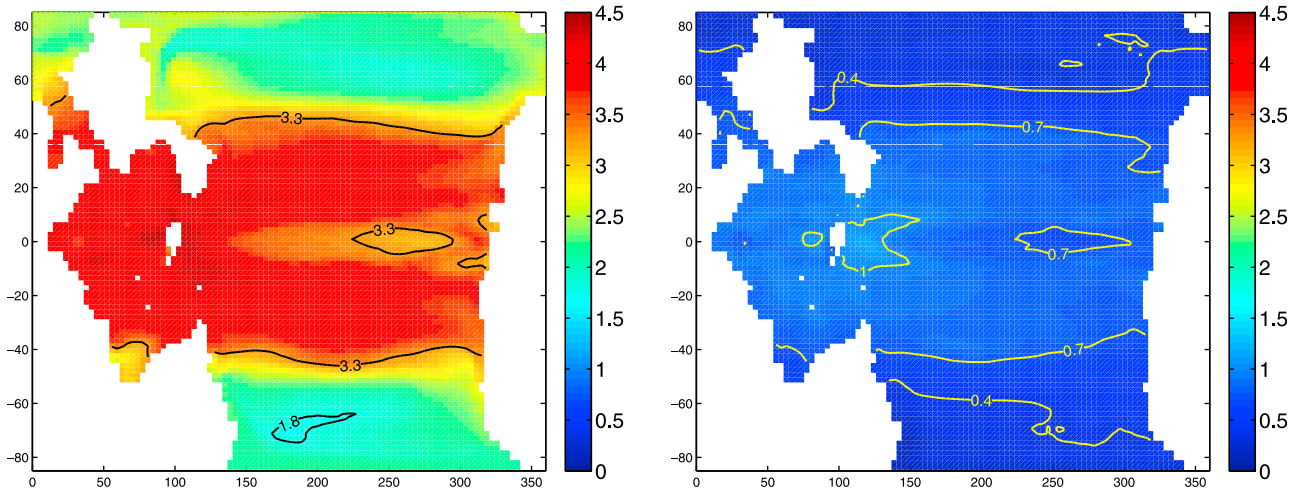

Figure 14. Annual mean ocean surface aragonite saturation. (left) Experiment 1xPD_O_FL; saturation of 3.3 is the lower limit of present-day reef-forming corals. (right) Experiment 10xPD_O_FL; the maximum saturation level for this simulation is 1.15.

al., 1996] and future projections point to, among other changes, significant surface ocean acidification over the next decades [*Caldeira and Wickett*, 2003]. In Figure 16 we compare our Permian results to present-day and predicted values of dissolved inorganic carbon (DIC) and surface pH modeled by the UVic ESCM. Climate at year 2100 is based on an A2 emission scenario [*Nakicenovic et al.*, 2000]. Our 1xPD surface pH is higher that what is modeled for the present day, particularly at high latitudes. While the predicted decrease in pH between years 2000 and 2100 is significant, modeled surface pH at the end of the present century is still on average 9% larger than our modeled 10xPD values. The reduction in modeled surface pH between years 2000 and 2100 is about 1/3 of the decrease registered between our 1xPD and 10xPD simulations (Figure 16). The modeled global DIC at year 2100 also stands between present-day values and our PTB estimates. As expected, the observed increase in DIC at year 2100 is maximum at the surface and decreases with depth.

5. Conclusions

[52] We use a Permian-Triassic boundary version of the UVic ESCM to evaluate ocean anoxia and surface ocean carbonate chemistry during the period. Experiments were forced by two distinct paleogeographies, three different ocean bottom topographies and atmospheric CO_2 concentrations of 300, 3000 and 4500 ppmv. The modeled temperatures of the high CO_2 simulations are in good agreement with reconstructions, and our simulations produce spatial distribution of temperature, snow cover and sea ice at southern high latitudes that match reconstructions better than previous EMIC modeling efforts. Modeled precipitation-evaporation is also in general agreement with climate sensitive sediments and there is good agreement

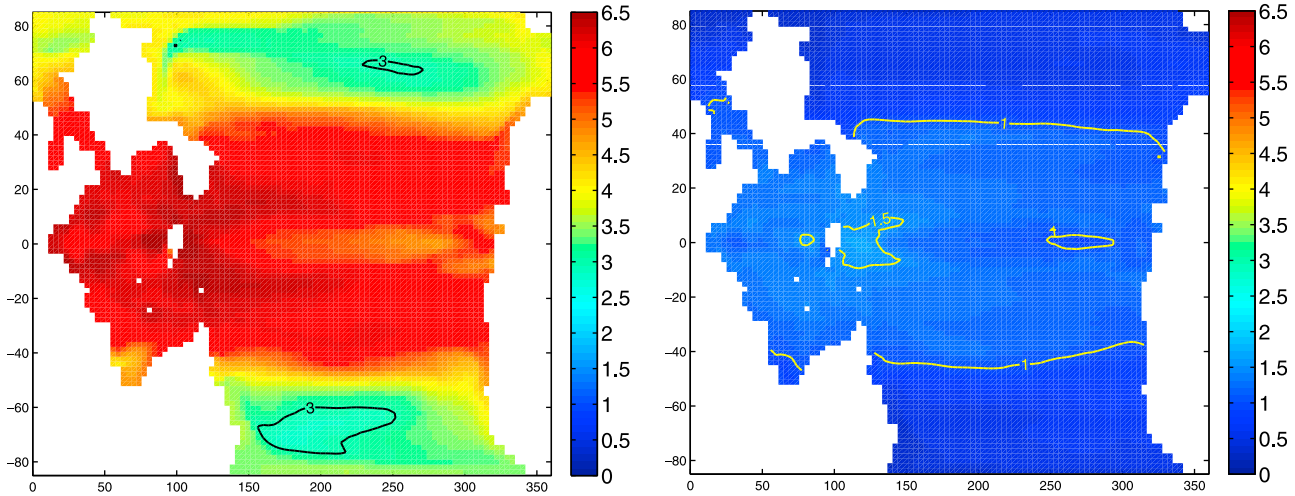

Figure 15. Annual mean ocean surface calcite saturation. (left) Experiment 1xPD_O_FL; the minimum saturation level for this simulation is 2.77. (right) Experiment 10xPD_O_FL; the maximum saturation level for this simulation is 1.69.

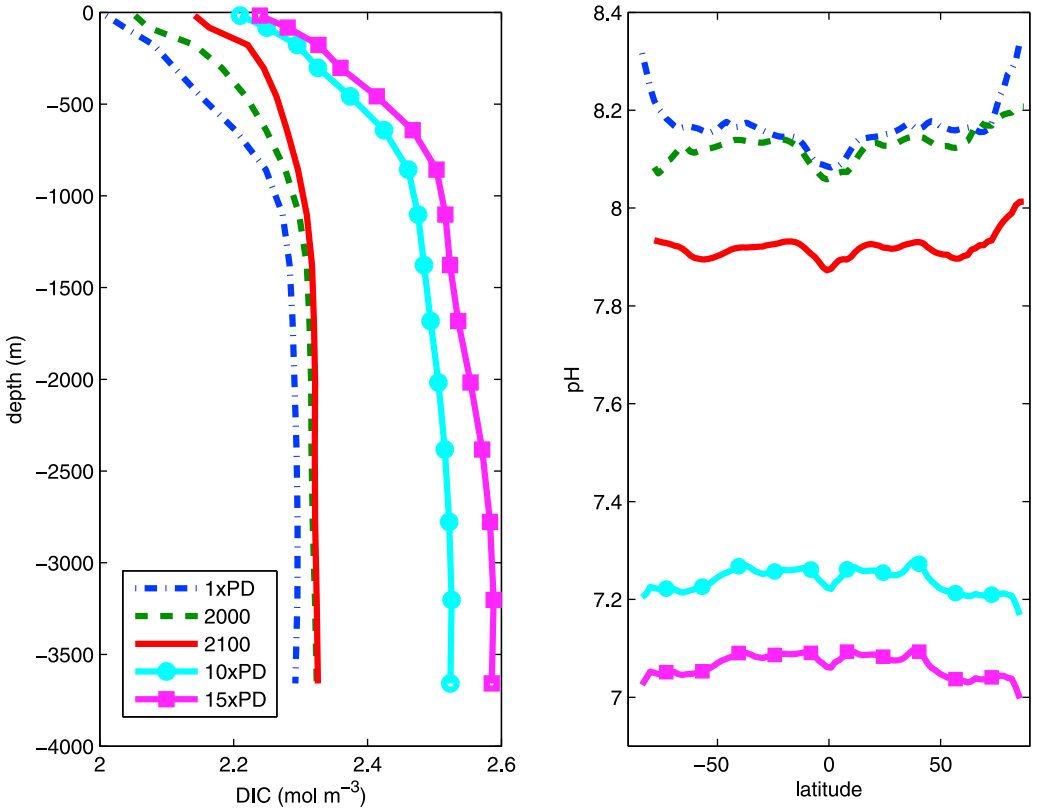

Figure 16. Comparison of modeled PTB DIC and surface pH to present-day values and future predictions. (left) Global, annual mean DIC vertical profiles. The 1xPD and 10xPD lines are an average of the open and closed gateway experiments, and the 15xPD refer only to the open gateway. All PTB data are from flat bottom experiments. The 2000 curve refers to data at the year 2000 from a historical simulation of the UVic ESCM, and the 2100 curve refers to data from a projection at year 2100 of the same model based on an A2 emissions scenario. (right) Zonally averaged annual mean values of surface ocean pH for the same experiments.

between modeled vegetation and reconstructed biomes for the middle-to-Late Permian, with the 15xPD simulation generating a slightly better match.

[53] Modeled deep ocean O_2 concentrations are high and not significantly impacted by changes in paleogeography and bathymetry. This seems contrary to observations that point to widespread bottom anoxia during the PTB. Our overturning circulation is similar or weaker than those of earlier EMIC simulations, but stronger than the overturning generated by an AOGCM simulation of the period. We take this as an indication that the dynamic coupling between ocean and atmosphere might be an important mechanism in the establishment of stagnant conditions during the PTB. The presence of ridges increased the strength of our modeled MOC. It would be interesting to verify if the same occurs in AOGCM simulations, and how this would impact modeled anoxia in those types of models. Another possible explanation for this discrepancy between our oxygen results and the proxy data is that Permian anoxia might not have been brought about exclusively by changes in ocean dynamics in a high CO_2 world, but might also have been related to alterations in ocean nutrient content and/or utilization.

[54] While no general bottom anoxia is reproduced, our results can not, for the reasons discussed above, be used as evidence against this extinction mechanism. However, our simulations offer support to the argument that a change in ocean dynamics resulting from climate warming is not sufficient by itself to generate widespread anoxic conditions during the PTB. It is worth noting that modeled midlevel (~200–1000 m) anoxia increased significantly under higher CO_2.

[55] The modeled aragonite saturation levels of the high CO_2 experiments are low enough to make the whole ocean unsuitable to present-day corals, which precipitate the same form of calcium carbonate as important Late Permian reef builders. Large areas of the ocean are unsaturated in relationship to calcite in the 10xPD experiments and essentially the whole surface ocean of the 15xPD simulation has calcite saturation levels below one.

[56] **Acknowledgments.** The authors would like to thank C. Shields for her generous help with the wind and topographic data. The manuscript was greatly improved by insightful comments from C. Shields, P. Wignall, R. Zahn, and an anonymous reviewer, for which the authors are thankful. A.M., M.J.M., and S.T.J. are grateful for funding received from NSERC; K.J.M. is grateful for funding from the Australian Research Council's Future Fellowship scheme.

References

Beauchamp, B., and A. Baud (2002), Growth and demise of Permian biogenic chert along northwest Pangea: Evidence for end-Permian collapse

of thermohaline circulation, *Palaeogeogr. Palaeoclimatol. Palaeoecol.*, *184*, 37–63.

Berner, R. (2002), Examination of hypotheses for the Permo-Triassic boundary extinction by carbon cycle modeling, *Proc. Natl. Acad. Sci. U. S. A.*, *99*, 4172–4177.

Berner, R., and K. Zavareth (2001), GEOCARB III: A revised model of atmospheric CO_2 over Phanerozoic time, *Am. J. Sci.*, *301*, 182–204.

Blakey, R. (2003), Carboniferous-Permian paleogeography of the assembly of pangaea, in *Proceedings of the XVth International Congress on Carboniferous and Permian Stratigraphy*, edited by T. E. Wong, pp. 433–456, R. Neth. Acad. of Arts and Sci., Amsterdam.

Bond, D., and P. Wignall (2010), Pyrite framboid study of marine Permian-Triassic boundary sections: A complex anoxic event and its relationship to contemporaneous mass extinction, *Geol. Soc. Am. Bull.*, *122*, 1265–1279, doi:10.1130/B30042.1.

Bowring, S., D. H. Erwin, Y. G. Jin, M. Martin, K. Davidek, and W. Wang (1998), U/pb zircon geochronology and tempo of the end-Permian mass extinction, *Science*, *280*, 1039–1045.

Caldeira, K., and M. Wickett (2003), Anthropogenic carbon and ocean pH, *Nature*, *425*, 365.

Campbell, I., G. Czamanske, V. Fedorenko, R. Hill, and V. Stepanov (1992), Synchronism of the siberian traps and the Permian-Triassic boundary, *Science*, *258*, 1760–1763.

Clarke, A. (1993), Temperature and extinction in the sea: A physiologist's view, *Paleobiology*, *19*(4), 499–518.

Collins, W. J. (2003), Slab pull, mantle convection, and pangaean assembly and dispersal, *Earth Planet. Sci. Lett.*, *205*, 225–237.

Cox, P. (2001), Description of the "TRIFFID" dynamic global vegetation model, *Tech. Note 24*, Hadley Cent., Met Off., Exeter, U. K.

Eby, M., K. Zickfeld, A. Montenegro, D. Archer, K. J. Meissner, and A. J. Weaver (2009), Lifetime of anthropogenic climate change: Millennial time scales of potential CO_2 and surface temperature perturbations, *J. Clim.*, *22*(10), 2501–2511, doi:10.1175/2008JCLI2554.1.

Erwin, D. (1994), The Permo-Triassic extinction, *Nature*, *367*, 231–235.

Fluteau, F., J. Besse, J. Broutin, and G. Ramstein (2001), The Late Permian climate. What can be inferred from climate modelling concerning Pangea scenarios and Hercynian range altitude?, *Palaeogeogr. Palaeoclimatol. Palaeoecol.*, *167*, 39–71.

Garcia, H. E., R. A. Locarnini, T. P. Boyer, and J. I. Antonov (2006), *World Ocean Atlas* 2005, vol. 3, *Dissolved Oxygen, Apparent Oxygen Utilization, and Oxygen Saturation*, *NOAA Atlas NESDIS*, vol. 63, edited by S. Levitus, 342 pp., NOAA, Silver Spring, Md.

Gibbs, M., P. Rees, J. Kutzbach, A. Ziegler, P. Behling, and D. Rowley (2002), Simulations of Permian climate and comparisons with climate-sensitive sediments, *J. Geol.*, *110*, 33–55.

Guinotte, J., and V. J. Fabry (2008), Ocean acidfication and its potential effects on marine ecosystems, *Ann. N. Y. Acad. Sci.*, *1134*, 320–342, doi:10.1196/annals.1439.013.

Gruber, N., J. L. Sarmiento, and T. Stocker (1996), An improved method for detecting anthropogenic CO_2 in the oceans, *Global Biogeochem. Cycles*, *10*, 809–837.

Heydari, E., J. Hassanzadeh, W. Wade, and A.M.Ghazi (2003), Permian-Triassic boundary interval in the Abadeh section of Iran with implications for mass extinction: Part 1 - Sedimentology, *Palaeogeogr. Palaeoclimatol. Palaeoecol.*, *193*, 405–423, doi:10.1016/S0031-0182(03)00258-X.

Heydari, E., N. Arzani, and J. Hassanzadeh (2008), Mantle plume: The invisible serial killer - Application to the Permian-Triassic boundary mass extinction, *Palaeogeogr. Palaeoclimatol. Palaeoecol.*, *264*, 147–162.

Hotinski, R., K. Bice, L. Kump, R. Najjar, and M. Arthur (2001), Ocean stagnation and end-Permian anoxia, *Geology*, *29*, 7–10.

Isozaki, Y. (1997), Permo-triassic boundary superanoxia and stratified superocean: Records from lost deep sea, *Science*, *276*, 235–238.

Johnston, S. T., and G. D. Borel (2007), The odyssey of the Cache Creek terrane, Canadian Cordillera: Implications for accretionary orogens, tectonic setting of Panthalassa, the Pacific superwell, and break-up of Pangea, *Earth Planet. Sci. Lett.*, *253*, 415–438.

Jones, A. T., T. D. Frank, and C. R. Fielding (2006), Cold climate in the eastern Australian mid to late Permian may reflect cold upwelling waters, *Palaeogeogr. Palaeoclimatol. Palaeoecol.*, *237*, 370–377, doi:10.1016/j.palaeo.2005.12.009.

Kakuwa, Y. (2008), Evaluation of palaeo-oxygenation of the ocean bottom across the Permian-Triassic boundary, *Global Planet. Change*, *63*, 40–56, doi:10.1016/j.gloplacha.2008.05.002.

Kato, Y., K. Nakao, and Y. Isozaki (2002), Geochemistry of late permian to early triassic pelagic cherts from southwest japan: implications for an oceanic redox change, *Chem. Geol.*, *182*, 15–34.

Kidder, D., and T. Worsley (2004), Causes and consequences of extreme Permo-Triassic warming to globally equable climate and relation to the Permo-Triassic extinction and recovery, *Palaeogeogr. Palaeoclimatol. Palaeoecol.*, *203*, 207–237.

Kiehl, J., and C. Shields (2005), Climate simulation of the latest Permian: Implications for mass extinction, *Geology*, *33*, 757–760, doi:10.1130/G21654.1.

Kleypas, J., J. McManus, and L. M. Menez (1999), Environmental limits to coral reef development: Where do we draw the line?, *Am. Zool.*, *39*, 146–159.

Kleypas, J., R. Feely, V. Fabry, C. Langdon, C. Sabine, and L. Robbins (2006), Impacts of ocean acidification on coral reefs and other marine calcifiers: A guide for future research, report, NOAA, Silver Spring, Md.

Knoll, A., R. Bambach, D. Canfield, and J. Grotzinger (1996), Comparative earth history and late permian mass extinction, *Science*, *273*, 452–457.

Kump, L., A. Pavlov, and M. A. Arthur (2005), Massive release of hydrogen sulfide to the surface ocean and atmosphere during intervals of oceanic anoxia, *Geology*, *33*, 397–400.

Kutzbatch, J., and A. Ziegler (1993), Simulation of late Permian climate and biomes with an atmosphere-ocean model: Comparisons with observations, *Philos. Trans. R. Soc. London B*, *341*(1297), 327–340.

Manabe, S., and K. Bryan Jr. (1985), CO_2-induced change in a coupled ocean-atmosphere model and its paleoclimatic implications, *J. Geophys. Res.*, *90*, 11,689–11,707.

Matthews, H. D., A. J. Weaver, K. J. Meissner, N. P. Gillett, and M. Eby (2004), Natural and anthropogenic climate change: Incorporating historical land cover change, vegetation dynamics and the global carbon cycle, *Clim. Dyn.*, *22*, 461–479.

McElwain, J. S. P. (2007), Mass extinction events and the plant fossil record, *Trends Ecol. Evol.*, *22*(10), 548–557, doi:10.1016/j.tree.2007.09.003.

Meissner, K. J., A. J. Weaver, H. D. Matthews, and P. M. Cox (2003), The role of land-surface dynamics in glacial inception: A study with the UVic Earth System Model, *Clim. Dyn.*, *21*, 515–537.

Meyer, K., and L. Kump (2008), Oceanic euxinia in earth history: Causes and consequences, *Annu. Rev. Earth Planet. Sci.*, *36*, 251–288.

Meyer, K., L. Kump, and A. Ridgwell (2008), Biogeochemical controls on photic-zone euxinia during the end-permian mass extinction, *Geology*, *36*, 747–750.

Nakicenovic, N., et al. (2000), Emission Scenarios: Special Report of Working Group III of the Intergovernmental Panel on Climate Change, edited by N. Nakicenovic and R. Swart, Cambridge Univ. Press, Cambridge, U. K.

Pacanowski, R. (1996), MOM2, version 2.0 Beta: Documentation, user's guide and reference manual, *GFDL Ocean Tech. Rep. 3.2*, Geophys. Fluid, Dyn. Lab., Princeton, N. J.

Payne, J. L., D. J. Lehrmann, D. Follet, M. Siebel, L. R. Kump, A. Riccardi, D. Altiner, H. Sano, and J. Wei (2007), Erosional truncation of uppermost Permian shallow-marine carbonates and implications for Permian-Triassic boundary events, *Geol. Soc. Am. Bull.*, *119*, 771–784.

Poussart, P., A. Weaver, and C. Barnes (1999), Late Ordovician glaciation under high atmospheric CO_2: A coupled model analysis, *Paleoceanography*, *14*, 542–558.

Rampino, M., A. Prokoph, and A. Adler (2000), Tempo of the end-permian event: high resolution cyclostratigraphy at the Permian-Triassic boundary, *Geology*, *28*, 643–646.

Rees, P. M. (2002), Land diversity and the end-Permian extinction, *Geology*, *30*, 827–830.

Rees, P. M., M. T. Gibbs, A. M. Ziegler, J. E. Kutzbach, and P. J. Behling (1999), Permian climates: Evaluating model predictions using global paleobotanical data, *Geology*, *27*, 891–894.

Rees, P. M., A. M. Ziegler, M. T. Gibbs, J. E. Kutzbach, P. J. Behling, and D. B. Rowley (2002), Permian phytogeographic patterns and climate data/model comparisons, *J. Geol.*, *110*, 1–31.

Reynaud, S., N. Leclercq, S. Romaine-Lioud, C. Ferrier-Pages, J. Jaubert, and J. Gattuso (2003), Interacting effects of CO_2 partial pressure and temperature on photosynthesis and calcification in a scleractinian coral, *Global Change Biol.*, *9*, 1660–1668, doi:10.1046/j.1529-8817.2003.00678.x.

Sarmiento, J., T. Herbert, and J. Togweiler (1988), Causes of anoxia in the world ocean, *Global Biogeochem. Cycles*, *2*, 115–128.

Schmittner, A., K. J. Meissner, M. Eby, and A. J. Weaver (2002), Forcing of the deep ocean circulation in simulations of the Last Glacial Maximum, *Paleoceanography*, *17*(2), 1015, doi:10.1029/2001PA000633.

Schmittner, A., A. D. Matthews, and E. D. Galbraith (2008), Future changes in climate, ocean circulation, ecosystems and biogeochemical cycling simulated for a business-as-usual CO_2 emission scenario until year 4000 AD, *Global Biogeochem. Cycles*, *22*, GB1013, doi:10.1029/2007GB002953.

Sengör, A. M. C. (1984), *The Cimmeride Orogenic System and the Tectonics of Eurasia*, *Spec. Pap. Geol. Soc. Am.*, *195*, 82 pp.

Sengör, A. M. C., B. Natalín, and V. Burtman (1993), Evolution of the Altaid tectonic collage and Palaeozoic crustal growth in Eurasia, *Nature*, *364*, 299–307.

Stampfli, G. M., and G. D. Borel (2002), A plate tectonic model for the paleozoic and mesozoic constrained by dynamic plate boundaries and restored synthetic oceanic isochrons, *Earth Planet. Sci. Lett.*, *196*, 17–33.

Stanley, S. (2008), Effects of global seawater chemistry on biomineralization: Past, present, and future, *Chem. Rev.*, *108*, 4483–4498.

Twitchett, R., C. Looy, R. Morante, H. Visscher, and P. Wignall (2001), Rapid and synchronous collapse of marine and terrestrial ecosystems during the end-permian biotic crisis, *Geology*, *29*, 351–354.

Weaver, A. J., et al. (2001), The UVic Earth System Climate Model: Model description, climatology and application to past, present and future climates, *Atmos. Ocean*, *39*, 361–428.

Wignall, P. B. (2007), The End-Permian mass extinction how bad did it get?, *Geobiology*, *5*, 303–309, doi:10.1111/j.1472-4669.2007.00130.x.

Wignall, P. B., and R. J. Twitchett (1996), Oceanic anoxia and the end Permian mass extinction, *Science*, *272*, 1155–1158.

Wignall, P. B., D. Bond, K. Kuwahara, Y. Kakuwa, R. Newton, and S. Poulton (2010), An 80 million year oceanic redox history from Permian to Jurassic pelagic sediments of the Mino-Tamba terrane, SW Japan, and the origin of four mass extinctions, *Global Planet. Change*, *71*, 109–123, doi:10.1016/j.gloplacha.2010.01.022.

Winguth, A., and E. Maier-Reimer (2005), Causes of the marine productivity and oxygen changes associated with the Permian-Triassic boundary: A reevaluation with ocean general circulation models, *Mar. Geol.*, *217*, 283–304, doi:10.1016/j.margeo.2005.02.011.

Winguth, A. M. E., C. Heinze, J. E. Kutzbach, E. Maier-Reimer, U. Mikolajewicz, D. Rowley, A. Rees, and A. M. Ziegler (2002), Simulated warm polar currents during the middle Permian, *Paleoceanography*, *17*(4), 1057, doi:10.1029/2001PA000646.

Yin, H., Q. Feng, X. Lai, A. Baud, and J. Tong (2007), The protracted permo-triassic crisis and multi-episode extinction around the Permian-Triassic boundary, *Global Planet. Change*, *55*, 1–20.

Zhang, R., M. Follows, J. Grotzingearn, and J. Marshall (2001), Could the late Permian deep ocean have been anoxic?, *Paleoceanography*, *16*, 317–329.

Ziegler, A., M. Gibbs, and M. Hulver (1988), A mini-atlas of oceanic water masses in the Permian period, *Proc. R. Soc. Vic.*, *110*, 323–343.

M. Eby and S. T. Johnston, School of Earth and Ocean Sciences, University of Victoria, PO Box 3055, Victoria, BC V8W 3P6, Canada.

K. J. Meissner and P. Spence, Climate Change Research Centre, Level 4, Mathews Building, University of New South Wales, Sydney, NSW 2052, Australia.

M. J. Melchin, Department of Earth Sciences, St. Francis Xavier University, Physical Sciences Complex, 1 West St., Antigonish, NS B2G 2W5, Canada.

A. Montenegro, Environmental Sciences Research Centre, St. Francis Xavier University, Physical Sciences Complex, 1 West St., Antigonish, NS B2G 2W5, Canada. (a.montenegro@stfx.ca)